Monthly Notices of the ROYAL ASTRONOMICAL SOCIETY

MNRAS **526,** 4174–4191 (2023) https://doi.org/10.1093/mnras/stad2989
Advance Access publication 2023 October 3

Signatures of feedback in the spectacular extended emission region of NGC 5972

Thomas Harvey [1,2,3★] W. Peter Maksym,[1] William Keel [4] Michael Koss [5,6] Vardha N. Bennert,[7] S. Drew Chojnowski,[8] Ezequiel Treister,[9] Carolina Finlez,[9] Chris J. Lintott [10] Alexei Moiseev [11] Brooke D. Simmons [12] Lia F. Sartori[13] and Megan Urry[14,15]

[1]*Center for Astrophysics | Harvard & Smithsonian, 60 Garden Street, Cambridge, MA 02138, USA*
[2]*Physics and Astronomy, University of Southampton, Southampton SO17 1BJ, UK*
[3]*Jodrell Bank Centre for Astrophysics, University of Manchester, Oxford Road, Manchester M13 9PL, UK*
[4]*Department of Physics and Astronomy, University of Alabama, 206 Gallalee Hall, 514 University Blvd. Tuscaloosa, AL 35487-0324, USA*
[5]*Space Science Institute, 4765 Walnut Street, Suite 205, Boulder, CO 80301, USA*
[6]*Eureka Scientific, 2452 Delmer Street Suite 100, Oakland, CA 94602-3017, USA*
[7]*Physics Department, California Polytechnic State University, San Luis Obispo, CA 93407, USA*
[8]*Department of Astronomy, New Mexico State University, Las Cruces, NM 88001, USA*
[9]*Instituto de Astrofísica, Facultad de Física, Pontificia Universidad Católica de Chile, Casilla 306, Santiago 22, Chile*
[10]*Department of Physics, University of Oxford, Denys Wilkinson Building, Keble Road, Oxford OX1 3RH, UK*
[11]*Special Astrophysical Observatory, Nizhny Arkhyz 369167, Russia*
[12]*Physics Department, Lancaster University, Lancaster LA1 4YB, UK*
[13]*Institute for Particle Physics and Astrophysics, Department of Physics, ETH Zurich, Wolfgang-Pauli-Strasse 27, CH-8093 Zurich, Switzerland*
[14]*Physics Department, Yale Center for Astronomy and Astrophysics, PO Box 208120, New Haven, CT 06520, USA*
[15]*Department of Physics, Yale University, PO Box 208121, New Haven, CT 06520, USA*

Accepted 2023 September 29. Received 2023 September 25; in original form 2022 August 12

ABSTRACT

We present *Chandra X-ray Observatory* observations and Space Telescope Imaging Spectrograph spectra of NGC 5972, one of the 19 'Voorwerpjes' galaxies. This galaxy contains an extended emission-line region (EELR) and an arcsecond scale nuclear bubble. NGC 5972 is a faded active galactic nucleus (AGN), with EELR luminosity suggesting a 2.1 dex decrease in $L_{\rm bol}$ in the last $\sim 5 \times 10^4$ yr. We investigate the role of AGN feedback in exciting the EELR and bubble given the long-term variability and potential accretion state changes. We detect broad-band (0.3–8 keV) X-ray emission in the near-nuclear regions, coincident with the [O III] bubble, as well as diffuse soft X-ray emission coincident with the EELR. The soft nuclear (0.5–1.5 keV) emission is spatially extended and the spectra are consistent with two APEC thermal populations ($\sim$0.80 and $\sim$0.10 keV). We find a bubble age $>$2.2 Myr, suggesting formation before the current variability. We find evidence for efficient feedback with $P_{\rm kin}/L_{\rm bol} \sim 0.8$ per cent, which may be overestimated given the recent $L_{\rm bol}$ variation. [O III] kinematics show a 300 km s^{-1} high-ionization velocity consistent with disturbed rotation or potentially the line-of-sight component of a $\sim$780 km s^{-1} thermal X-ray outflow capable of driving strong shocks to photoionize the precursor material. We explore possibilities to explain the overall jet, radio lobe and EELR misalignment including evidence for a double supermassive black hole which could support a complex misaligned system.

Key words: galaxies: active – galaxies: individual: NGC5972 – galaxies: ISM – galxies: Seyfert – X-rays: galaxies.

1 INTRODUCTION

Active galactic nuclei (AGNs) are thought to play an important role in the evolution of their host galaxy through their interaction with the interstellar medium (ISM) via winds, outflows, and jets (see reviews by Alexander & Hickox 2012; Fabian 2012). In many galaxies, direct photo-ionization by AGN emission only extends to the narrow-line region (NLR) within a kiloparsec of the supermassive black hole (SMBH, see e.g Elvis 2000; Bennert et al. 2002). However, there is a long-known population of galaxies which display the same distinct ionization signatures on a much larger spatial scale; firstly surrounding radio-loud galaxies and quasars (see review by Stockton, Fu & Canalizo 2006), but more recently near lower luminosity AGN as well. These extended emission-line regions (EELRs) contain AGN-ionized warm gas at scales larger than 10 kpc from the AGN (see Lintott et al. 2009; Schawinski et al. 2010; Keel et al. 2012b, 2017). These EELRs have been used as light echos to probe AGN variability on previously inaccessible kyr time-scales.

1.1 AGN feedback

The interaction of outflows with the fuel supply of the AGN causes a feedback loop which self-regulates SMBH growth and star formation

★ E-mail: thomas.harvey-3@manchester.ac.uk

© 2023 The Author(s)
Published by Oxford University Press on behalf of Royal Astronomical Society. This is an Open Access article distributed under the terms of the Creative Commons Attribution License (http://creativecommons.org/licenses/by/4.0/), which permits unrestricted reuse, distribution, and reproduction in any medium, provided the original work is properly cited.

Downloaded from https://academic.oup.com/mnras/article/526/3/4174/7288715 by Cal Polytechnic State Univ San Luis Obispo user on 29 November 2023

(Silk & Rees 1998; Di Matteo, Springel & Hernquist 2005), known as AGN feedback. Infalling gas sets off a period of rapid, radiatively efficient, high Eddington ratio accretion until feedback from outflows entrains the infalling gas, choking the fuel supply, and reducing the accretion rate and luminosity (e.g. Shankar, Weinberg & Miralda-Escudé 2009). These duty cycles of high and low accretion, which we call AGN 'state changes', may be analogous to observations of accretion in X-ray binaries (XRBs) where we observe rapid accretion rate variability on much shorter time-scales (see e.g. Maccarone, Gallo & Fender 2003; Körding, Jester & Fender 2006; McHardy et al. 2006; Eckersall, Vaughan & Wynn 2015). The transition between states is thought to be linked to a decrease in the accretion rate (Remillard & McClintock 2006; Belloni 2010; Skipper & McHardy 2016), which correlates with an increase in kinetic power (Done, Gierliński & Kubota 2007) driving outflows and winds. This idea has been extended to AGN (see e.g. Alexander & Hickox 2012), where luminous AGN correspond to the soft state and low-luminosity AGN correspond to the hard state, where most of the energy output is kinetic. Many authors (McHardy et al. 2006; Schawinski et al. 2010), have suggested that during this inefficient, kinetically dominated accretion state the SMBHs perform significant feedback work on the ISM within their host galaxies. The periods of rapid efficient accretion are thought to last for around 10^5 yr, with fast state changes on the order of 10^4 yr (Keel et al. 2012b, 2017; Schawinski et al. 2015). The AGN flicker on and off for an overall total accretion time-scale of 10^{7-9} yr (e.g. Soltan 1982; Yu & Tremaine 2002). The mechanisms and effects of this feedback on the wider galaxy are not well understood. We have known for some time that the masses of SMBH are correlated with properties of their host galaxies (e.g. Magorrian et al. 1998; Gebhardt et al. 2000; Hopkins et al. 2007) and it is thought that this feedback interaction leads to these correlations (Silk & Rees 1998; Fabian 1999).

Hopkins & Elvis (2009) have suggested a two-stage model for AGN feedback, where small high velocity outflows interacting with the diffuse warm/hot ISM cause additional feedback effects that lead to the dissipation of the cold ISM on large scales. The cold ISM is primarily composed of dense molecular clouds, which are the primary reservoir for star formation (e.g. McKee & Ostriker 1977). This idea reduces the kinetic output of the AGN required to unbind the ISM (and halt star formation) by an order of magnitude compared to conventional feedback models (e.g. Mathur et al. 2009). Hopkins & Elvis (2009) estimate around 0.5 per cent of $L_{\rm bol}$ is required for efficient feedback under this two-stage model. Given their long time-scale variation, it is difficult to identify faded AGN which may have enough kinetic power to meet this criterion. Galaxies which may have undergone recent extreme decreases in AGN luminosity are identified through the presence of quasar light echoes.

1.2 Quasar light echoes

The first such example is Hanny's Voorwerp (HV, Lintott et al. 2009), which is a large cloud of AGN-ionized gas known as an EELR. Analysis by Lintott et al. (2009) and Keel et al. (2012a) find an energy imbalance between the line emission of the cloud and the absorbed emission of the nearby AGN IC 2497. The luminosity required to sustain the observed EELR emission is 50 times greater than the current bolometric luminosity based on *Wide-field Infrared Survey Explorer (WISE)* mid-infrared (mid-IR) observations, corresponding to a decrease in Eddington ratio from 0.35 to 0.007 in the last 100 kyr (Sartori et al. 2018). Given the separation of HV and the host galaxy and the recombination time-scale of the narrow-line emission (Keel et al. 2012a), this probes AGN variability on a time-scale of around 100 000 yr.

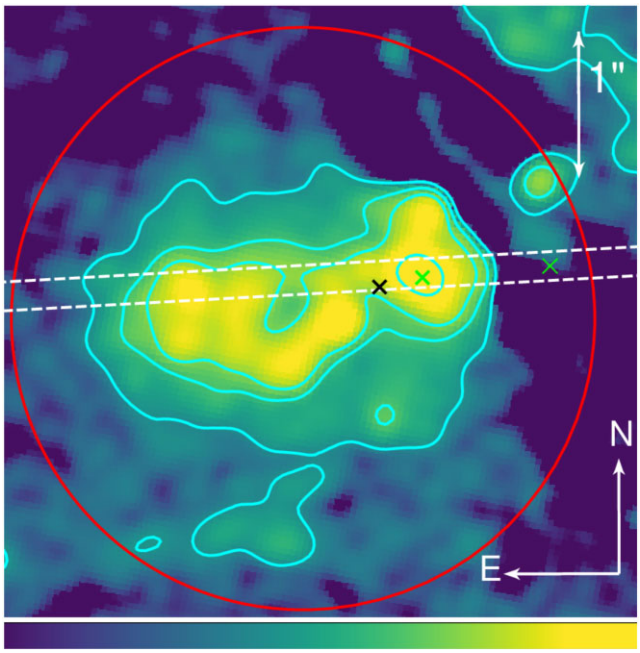

Figure 1. The STIS slit location for the observations detailed in Section 2.2.2, overlaid on the *HST* ACS WFC3 narrow-band [O III] image with a log scale. The inferred nuclear source location (detailed in Section 5.1) and the brightest [O III] region is shown by the central green cross. Logarithmic contours, with five contour levels and a dynamic range of 0.0015–0.01 photons s^{-1} cm^{-2} $pixel^{-1}$, are shown in blue. The red circle (2 arcsec radius) is the same as shown in other figures in Section 4.

NGC 5972 was identified in Sloan Digital Sky Survey (SDSS) imaging during a Galaxy Zoo search for signatures of faded AGN similar to IC 2497 (Keel et al. 2012b). Like IC 2497, NGC 5972 hosts an EELR containing significant amounts of extraplanar gas which is directly ionized by the AGN. NGC 5972 is a nearby ($z = 0.030$) Seyfert 2 galaxy which is thought to have faded dramatically in the last 50 000 yr. It has a radio luminosity at 1.4 GHz of $\approx 2 \times 10^{24}$ W Hz^{-1} (Condon et al. 1998), with a classic double-lobed radio structure separated by 330 kpc (Keel et al. 2012b). NGC 5972 hosts a powerful ($L \approx 1\,0^{44}$ erg s^{-1}), highly obscured ($\log N_{\rm H} = 24.34$, Zhao et al. 2021) AGN which powers a spectacular double helix-shaped [O III] emission structure. The EELR arms were originally identified as ionized gas and not a spiral galaxy by Veron & Veron-Cetty (1995). Keel et al. (2012b) note that the misalignment of the EELR and radio lobes by 67° is unusual for Seyfert galaxies. Keel et al. (2015) used *Hubble Space Telescope* (*HST*) imaging and supporting ground-based observations to investigate the morphology of NGC 5972 at subarcsecond resolution. They find evidence of a past merger consistent with a 1.5 Gyr-old precessing warped disc. The outermost parts of the EELR are located up to 50 kpc from the nucleus and follow the main disc rotation curve. In Keel et al. (2017), the luminosity history over the last 55 kyr is analysed, finding evidence for a 2.1 dex decrease in bolometric luminosity.

Keel et al. (2017) draw attention to an arcsecond scale [O III] structure, which hosts the central engine. They hypothesize that this feature, which does not show any velocity structure, is a loop or bubble of warm ionized gas. The authors speculate that the bubble is actually a signature of infalling gas rather than an AGN-driven outflow. Fig. 1 reproduces their [O III] image of this structure which we hereafter refer to as the '[O III] bubble' or just the 'bubble'.

Downloaded from https://academic.oup.com/mnras/article/526/3/4174/7288715 by Cal Polytechnic State Univ San Luis Obispo user on 29 November 2023

Table 1. Details of the *Chandra* ACIS-S observations used in this analysis.

Observation ID	Date	Total (useful) exposure (ks)	PI
18080	2016 Apr 04	9.83 (9.83)	Ajello
19562	2017 Dec 18	23.74 (23.6)	Maksym
20893	2017 Dec 19	23.73 (23.2)	Maksym
Merged		57.3 (56.6)	

In Zhao et al. (2021), analysis of Nuclear Spectroscopic Telescope Array (NuSTAR) and *Chandra X-Ray Observatory* observations was used to derive properties of the AGN and torus within NGC 5972. The authors fit the nuclear spectra with a physically motivated AGN model to constrain the AGN obscuration and orientation, finding a highly obscured, Compton-thick AGN ($\log N_{\rm H,\,tor} = 24.34$) which we observe through the obscuring torus.

NGC 5972 is the perfect laboratory for studying the effects of AGN feedback during a period of low Eddington rate accretion to test whether the feedback is efficient enough to halt star formation. We aim to understand the interaction and feedback effects between the hot gas in the bubble and the SMBH given the AGN state changes over the past 10^5 yr. In this paper, we present a new analysis of high-resolution *Chandra* X-ray imaging and spectroscopy of the AGN and EELR in NGC 5972. *Chandra*'s subarcsecond resolution allows us to study the interaction of the central engine and surrounding gas on small scales. We also use new *HST* Space Telescope Imaging Spectrograph (STIS) spectroscopy to investigate the kinematics of the gas within the [O III] bubble. Together these observations of the velocity, temperature and ionization source of gas within the [O III] bubble allow insights into the relationship between the nuclear SMBH and its environment.

This paper is organized as follows. In Section 2, the observations and data reduction process are described. In Section 3, we detail our methodology. The results are presented and discussed in Sections 4 and 5, respectively. Finally, we summarize our findings in Section 6.

For distances and angular sizes we adopt the cosmological parameters $H_0 = 70$ km s^{-1} Mpc^{-1}, $\Omega_{m,\,0} = 0.3$ and $\Omega_{\Lambda,\,0} = 0.7$. Emission-line wavelengths are given in vacuum and taken from the SDSS.[1]

2 OBSERVATIONS AND DATA REDUCTION

2.1 X-ray observations

Three observations of NGC 5972, totalling 55 ks, were obtained from the *Chandra* Data Archive.[2] These observations were taken using the Advanced CCD Imaging Spectrometer (ACIS), centred on the back-illuminated S3 chip within the ACIS-S array. The dates and lengths of these observations are given in Table 1. The observations were reduced using the Chandra Interactive Analysis of Observations (CIAO) package (Fruscione et al. 2006) versions 4.1.3 and 4.6.8 of the Chandra Calibration DataBase. The observations were reprocessed using the standard *CHANDRA_REPROCESS* script, followed by deflaring (using *DEFLARE*) to remove periods of high background at a confidence level of 3σ. NGC 5972 itself was excluded from the deflaring process. There were very few periods of high background, and the lengths of the total and useful observations are given in Table 1.

As is now the default option in CIAO, the observations were reprocessed to take advantage of the subpixel capabilities of the ACIS detector due to the spacecraft dither. The Energy Dependent Subpixel Event Repositioning algorithm (Li et al. 2004) can improve the spatial binning of the inferred event positions and fully sample the instrumental point spread function (PSF), increasing spatial resolution beyond the limitation imposed by the 0.492 arcsec detector pixels to 0.1–0.2 arcsec.

The individual observations were astrometrically aligned to the longest observation (ObsID 19562). First, the *FLUXIMAGE* tool was used to generate an image with 1/2 pixel binning (0.256 arcsec) from the event files, then a source list was extracted using *WAVDETECT*. The source lists were compared using *WCS_MATCH* and the astrometry of the event and aspect files were corrected using *WCS_UPDATE*. We allow only translational alignment of the images to avoid calibration issues with the aligned data products.

In order to identify as many sources as possible to obtain the best match we combine the observations using *merge_obs*and use the same process as above to align the merged event file to the Panoramic Survey Telescope and Rapid Response System Data Release 1 (Pan-STARRS DR1) catalogue (Chambers et al. 2016). The final reported root mean square offset between the extracted source list and the catalogue is 0.09 arcsec. This ensures we have a precise astrometric match to the *HST* imaging to allow comparison of small-scale features. The computed transform was then used to align each individual observation with the Pan-STARRS catalogue.

Table 2. Details of the *HST* observations used in this paper.

Filter/Grating	Date	Exposure (s)	PI
Imaging			
ACS FR505N	2012 July 01	2538	Keel
WFC3 F673N	2012 Dec 18	2890	Keel
Spectroscopy			
STIS G430L	2016 July 09	2071.8	Maksym
STIS G750M	2016 July 09	2854.8	Maksym

2.2 Optical data

2.2.1 *HST imaging*

HST imaging of NGC 5972 has been analysed extensively by Keel et al. (2015, 2017). They obtained emission-line images of the [O III] λ5008 line in the Advanced Camera for Surveys (ACS) FR505N ramp filter and Hα + [N II] images with Wide Field Camera 3 (WFC3) F673N narrow-band filter. Details of these observations are given in Table 2. We obtained these observations from the *Hubble* Legacy Archive and reduced them following the steps in Keel et al. (2015) to produce continuum subtracted and astrometrically matched images of NGC 5972 in flux units of photons cm^{-2} s^{-1}.

2.2.2 *HST spectroscopy*

Slit spectroscopy of NGC 5972 was taken during *HST* Cycle 23 (PI: W. P. Maksym, Proposal ID 14271). The sightline used was positioned to obtain spectra from the arcsecond scale [O III] bubble seen in the *HST* [O III] imaging. The slit location is shown in Fig. 1, with the slit centre located at RA 15:38:54.0760, Dec. +17:01:34.590 (shown by green cross on far right) at a position angle (PA) of 93°. The observations were taken using the STIS with gratings G430L and G750M. The slit used has an aperture of 52 arcsec × 0.2 arcsec. Details of the observations are given in Table 2. Each observation was split into three components for cosmic-ray rejection, but there is still

[1] http://classic.sdss.org/dr6/algorithms/linestable.html
[2] http://cda.harvard.edu/chaser

Downloaded from https://academic.oup.com/mnras/article/526/3/4174/7288715 by Cal Polytechnic State Univ San Luis Obispo user on 29 November 2023

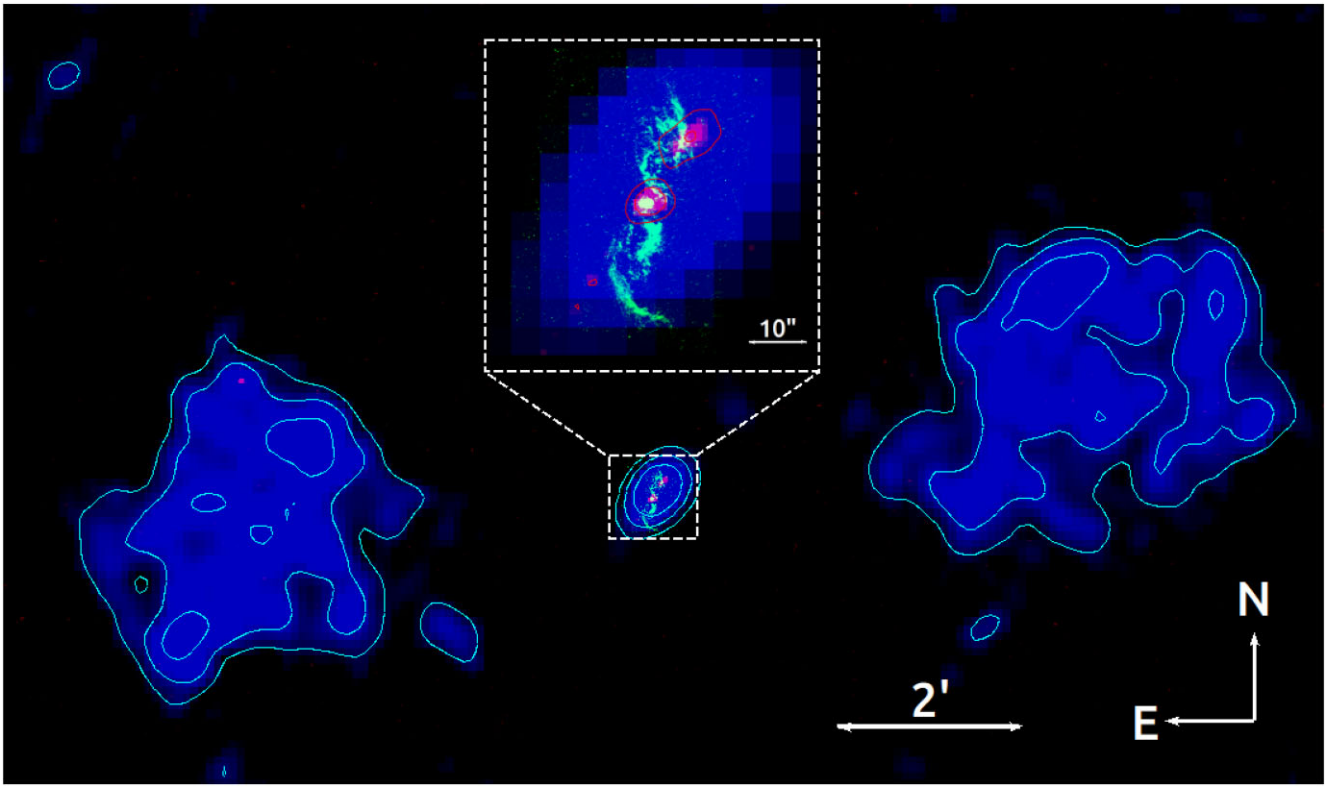

Figure 2. A three colour image of the radio and [O III] emission from NGC 5972. The blue and red channels show VLA observations at different wavelengths (VLASS 10 cm and VLA 20 cm, respectively) which are highlighted by logarithmic contours of the corresponding colour. The blue radio lobe contours have three levels with a dynamic range of 0.0007 to 0.003 Jy beam^{-1}, and the red contour shows one level of 0.0003 Jy beam^{-1} to indicate strong radio emission. The *HST* [O III] is shown in green for reference, and the cutout shows an enlarged view of the [O III] structure overlaid with the jet emission in red.

a high cosmic-ray background in the processed 2D spectra produced by the *Hubble* Legacy Archive's automated pipeline. To reduce this, we obtained the raw data files and used the PYTHON *ASTROSCRAPPY* (McCully et al. 2018) implementation of the L.A Cosmic algorithm (van Dokkum 2001) to remove cosmic rays. The tool was run with a threshold value of 5σ which removed most of the cosmic rays. The raw files were then processed using the *CALSTIS* script from the PYTHON package *STISTOOLS*[3] to produce cosmic-ray rejected 2D spectral images for each grating. Reprocessing the data also decreases the systematic uncertainties in the astrometry to <0.01 arcsec due to the addition of *Gaia* data into the pipeline.[4]

2.3 Radio data

As NGC 5972 has strong radio emission compared to other galaxies with EELRs (Keel et al. 2015), we obtained archival Very Large Array (VLA) observations in order to make comparisons between the X-ray, optical, and radio morphologies. A recent observation of the field containing NGC 5972 from the Very Large Array All Sky Survey was downloaded (VLASS, Lacy et al. 2020) using the Canadian Initiative for Radio Astronomy Data Analysis (CIRADA) Cutout service.[5] It was taken at a central wavelength of 10 cm on 2019 March 21 and has a resolution of 2.5 arcsec. We also obtain an archival 20-cm VLA observation from the National Radio Astronomy Observatory Archive[6] taken on 1986 November 26 (Condon et al. 1998) with a 45 arcsec full width at half-maximum (FWHM, Condon et al. 1998). For both observations, the default pipeline processing is suitable for our purposes as we are only interested in the bright, large scale morphology. Fig. 2 shows the 20 cm observation in blue, the VLASS 10 cm observation in red, and the *HST* [O III] image of NGC 5972 in green. The central cutout shows an enlarged view of the small-scale radio jet overlaid on the EELR features. The red (cyan) contours indicate the regions of strong radio emission in the 10 cm (20 cm) observation.

3 METHOD

3.1 *Chandra* imaging

We produced 1/4 pixel (0.124 arcsec) resolution images of NGC 5972 in the soft X-ray (0.3–2 keV), hard X-ray (2–8 keV), Fe Kα line (6–7 keV), and Ne IX line (0.865–0.938 keV). We have used the *dmimgadapt* algorithm to produce adaptively smoothed images where large-scale features are smoothed, while those on small scales are preserved. We produce adaptively smoothed images at both 3σ (9 counts) and 1σ (3 counts) to look for structure within the extended soft X-ray emission at different levels of significance.

In order to determine the nuclear source location, we look for the telltale strong Fe Kα line which is evidence of emission from

[3]https://stistools.readthedocs.io/en/latest/
[4]https://outerspace.stsci.edu/display/HAdP/Improvements+in+HST + Astrometry
[5]https://ws.cadc-ccda.hia-iha.nrc-cnrc.gc.ca/en/doc/data/
[6]https://data.nrao.edu/portal/

Downloaded from https://academic.oup.com/mnras/article/526/3/4174/7288715 by Cal Polytechnic State Univ San Luis Obispo user on 29 November 2023

the outer accretion disc and inner torus (Reynolds 2012; Gandhi, Hönig & Kishimoto 2015). This hard emission is expected to be a point-like source subject to *Chandra*'s PSF. The neutral iron line and other nuclear iron lines, (e.g. Fe XXV and Fe XXVI) emit between 6 and 7 keV. We limited the event file to this energy range and produced an image binned to 1/4 ACIS pixel resolution using DMCOPY. Our initial method was then to use the *wavdetect* to do source detection, generating an elliptical region centred on the peak of Fe Kα emission. We found issues with reproducibility leading to a modified method discussed in Section 5.1.

3.2 *Chandra* spectroscopy

3.2.1 Spectral extraction

In order to investigate the emission from the nucleus (coincident with the [O III] bubble) we extracted spectra from both a 0.25 and 2 arcsec radius apertures centred on the nuclear source location. The nuclear source location used is discussed in Section 5.1. A region of radius 6arcsec located 55 arcsec E of the nucleus was used to estimate the background. The *HST* [O III] image was used to define elliptical apertures covering the north and south EELRs. Fig. 4 shows these regions with dashed white ellipses. Spectra were extracted from these regions using the CIAO tool SPECEXTRACT following standard procedures and analysed using the PYTHON package SHERPA (Doe et al. 2007). Spectra were binned to 5 counts bin^{-1} to maximize the spectral resolution. The regions contained relatively few counts, between 15 and 300 depending on region and observation. For less than 25 counts bin^{-1}, the χ^2 statistic is unsuitable, and instead we use the *wstat* statistic from XSPEC. This statistic assumes that both the data and background obey a Poisson distribution and includes the background within the fit without modelling it. The same statistic and the SHERPA tool CONF are used to estimate the 1σ uncertainties in the best-fitting parameters. We refer to the 'reduced statistic', which is equivalent to the statistic divided by the number of degrees of freedom. This is equivalent to the traditional $\chi^2_{\rm red}$ for large counts bin^{-1}.

3.2.2 Spectral modelling of nucleus

The medium-hard X-ray emission from the nucleus of NGC 5972 has been modelled by Zhao et al. (2021) based on the archival *Chandra* X-ray data (1–7 keV) as well as NuSTAR data (3–78 keV). As NGC 5972 is Compton-thick, the harder energy range covered by NuSTAR is needed to constrain AGN properties such as the power-law slope. Extended emission from hot gas in the bubble and NLR is contaminated with emission from the central engine due to PSF spread. We have to constrain the emission from the AGN itself before we introduce models for the extended soft emission.

$$M = c_1 \times phabs_{gal} \times (borus02 + pl_{\rm cutoff} \times (phabs_{los} \times cabs_{los} + c_2)). \quad (1)$$

Zhao et al.'s (2021) XSPEC model, given in equation (1), consists of a physically motivated clumpy torus model derived from Monte Carlo simulations (borus02, Baloković, García & Cabral 2019) plus an absorbed cut-off power law ($pl_{\rm cutoff} \times phabs \times cabs$) and a small fractional constant representing unabsorbed reflected emission ($c_2 \times pl_{\rm cutoff}$). The *borus02* model models the reprocessing of the emission from the outer accretion disc and inner torus, while the obscured power-law models the line-of sight (LOS) absorption of the continuum. The entire model is multiplied by a *phabs* absorption component representing Galactic absorption from the local Milky Way ISM, with $N_{\rm H} = 3.12 \times 10^{20}$ cm^{-2} from the Colden Calculator (NRAO dataset, Dickey & Lockman 1990) in the CXC Proposal Planning Toolkit. They fit the X-ray emission from NGC 5972

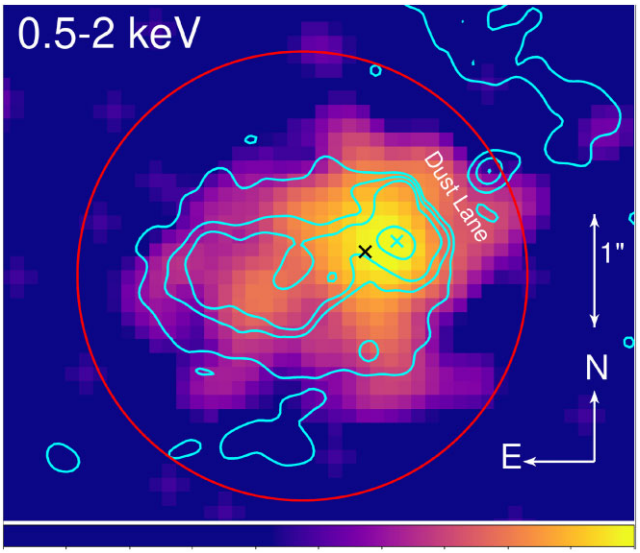

Figure 3. The smoothed soft (0.3–2 keV) X-ray observation binned to 1/4 ACIS-S pixel size of the central region of NGC 5972. The colour palette has been chosen to highlight the range of intensities across this region with a logarithmic scale, and the X-ray data are smoothed with a 3 pixel (3/4 ACIS pixel) Gaussian kernel. The spatially coincident *HST* [O III] observation is shown with blue contours, with five contour levels and a dynamic range of 0.0015–0.01 photons s^{-1} cm^{-2} pixel^{-1}. The red circle is the same as shown in Fig. 4 and the location of the SMBH is marked with a black cross. The labelled dust lane was identified by Keel et al. (2015) from *HST* imaging.

using an extraction region of radius 5 arcsec (75 arcsec) for *Chandra* (NuSTAR) observations. We freeze their best-fitting values for the following parameters; photon index $\Gamma = 1.75$; LOS column density log $N_{\rm H,\,los} = 23.79$; torus-averaged column density log $N_{\rm H,\,tor} = 23.34$; inclination angle $\cos(\theta_{\rm inc}) = 0.856$; and covering factor $c_f = 0.9$ in our model. First, we fit the hard emission (2–8 keV) within 0.25 arcsec of the central engine to fix the fractional constant which represents reflected emission and dominates between 2 and 4 keV. We then fit the spectra from the 2 arcsec bubble region for the same energy range to constrain the overall scaling factor of the AGN model, before introducing further model components to model the soft emission below 2 keV.

To characterize the soft emission, we explored combinations of the physically motivated models used for Mrk 573 by Paggi et al. (2012). This includes a component representing collisionally ionized diffuse gas (APEC, Smith et al. 2001) and the CLOUDY derived (Ferland et al. 1998) table model used by Paggi et al. (2012), which represents emission from gas photoionized by an AGN spectra. The CLOUDY model fits a grid of ionization parameters ($-2 \leq \log {\rm U} \leq 3$) and column densities ($19 \leq \log N_{\rm H} \leq 24$). The column density refers to the density of obscuring material between the ionized plasma and the AGN.

We fit the two longest and concurrent observations (ObsIDs 19562 and 20893) simultaneously and do not include the short, older observation as some of the model parameters (e.g. $N_{\rm H,\,los}$, the LOS column density) can be time-dependent.

3.2.3 Spectral modelling of EELRs

Fig. 4 shows the dashed white ellipses which indicate the regions used to extract the spectra of the north and south EELRs. We fit combinations of APEC and CLOUDY models multiplied by the Galactic

Downloaded from https://academic.oup.com/mnras/article/526/3/4174/7288715 by Cal Polytechnic State Univ San Luis Obispo user on 29 November 2023

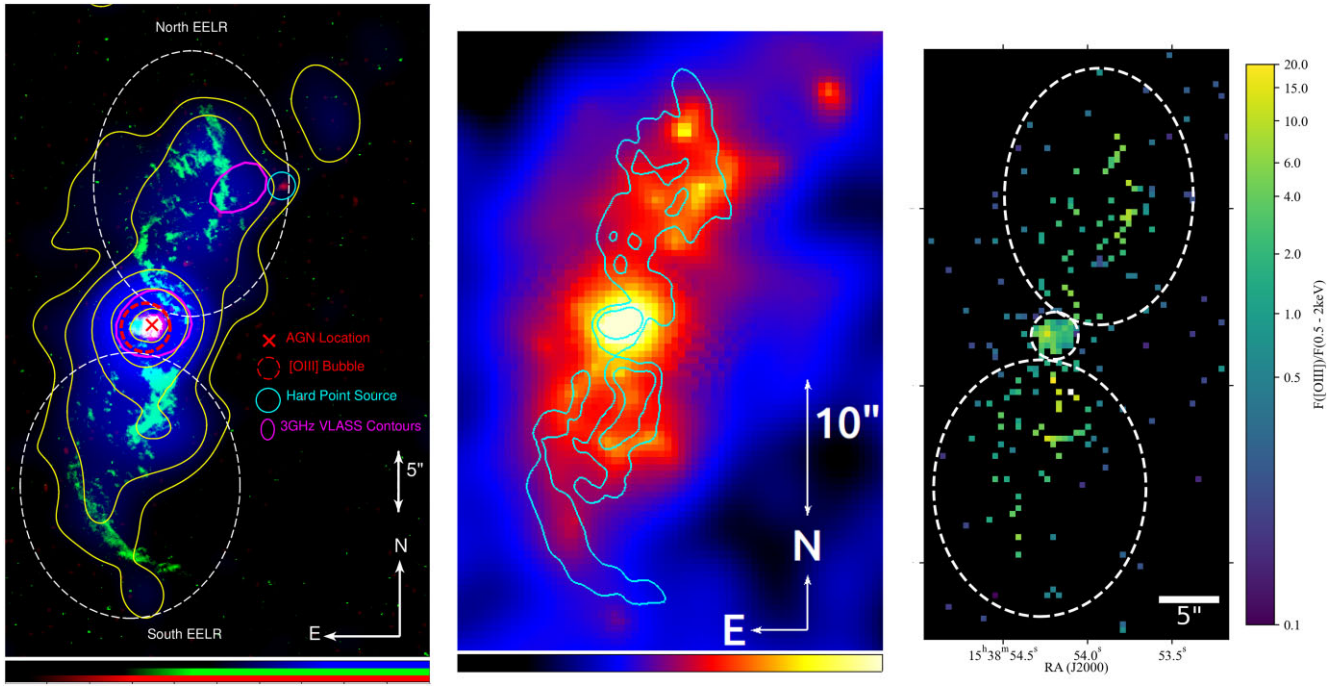

Figure 4. Left: the *HST* [O III] emission (green) overlaid with the soft (0.5–2 keV, blue), 3σ adaptively smoothed ACIS-S X-ray observation of NGC 5972. The red channel represents the hard (2–8 keV) emission smoothed with a 3 pixel Gaussian on a logarithmic scale. The logarithmically spaced contours (yellow) trace the soft emission, with five contour levels and a dynamic range of 0.01–0.5 counts cm^{-2} s^{-1} pixel^{-1}. The regions containing the EELRs are shown by dashed white ellipses, the [O III] bubble location is circled in red and the nuclear source location is shown with a red cross. The purple contours show the location of the radio emission based on the 3 GHz VLASS observation. Centre: the soft X-ray (0.5–2 keV) observation of NGC 5972, adaptively smoothed at 1σ, shown on a log scale. Cyan *HST* [O III] contours of 0.004 and 0.019 counts cm^{-2} s^{-1} are overlaid to show the correlation with the EELR. Right: the ratios of F([O III] λ5008) to F(0.3–2 keV) for the EELRs, binned to the native ACIS-S pixel size. Regions showing the location of the EELRs and [O III] bubble are overlaid for comparison. Black pixels indicate no X-ray flux.

absorption model (*phabs*) to the extracted spectra in the soft (0.3–2 keV) band. The north and south regions were fit separately and we fit only the two longest observations as the emission from the EELRs are not well constrained in the short 10 ks observations (ObsID 18080). We again bin the spectra to 5 counts bin^{-1} and use the wstat statistic due to the low numbers of total counts in each region.

3.3 *Chandra* PSF modelling

We followed the standard *Chandra* science threads[7] to simulate the PSF of each observation and energy band (0.5–1.5, 1.5–3, 3–6, and 6–7 keV) using the Chandra Ray Tracer (ChaRT) v2 (Carter et al. 2003). For the source spectrum, we used the Zhao et al. (2021) spectral model plus our best-fitting CLOUDY model of the soft X-ray emission below 2 keV. We simulate each observation individually as they have different off-axis angles and aspect solutions. We ran 1000 iterations of the simulation for each observation and energy band to ensure our PSF model was robust.

We used MARX (Davis et al. 2012) to project the simulated rays from CHaRT onto the detector and generate a PSF image. To test whether the apparent extent was real rather than an artefact of the PSF we extracted counts from both the observations and the simulated PSF images using CIAO's *dmextract* tool. We use concentric annuli with radii 0.3, 0.6, 0.9, 1.2, 1.5, 2, 2.5, and 3 arcsec centred on the nuclear source location. It is well documented that the *Chandra* PSF exhibits an asymmetry at small scales, and we exclude this region of higher counts using the *MAKE_PSF_ASYMMETRY_REGION* for each observation. The same background region as used in the spectral extractions is used here, and the uncertainties in the counts in each region are given by the Poisson distribution with $\sigma_N = \sqrt{N}$, or by the Gehrels approximation in the low count ($N \leq 25$) regime $\sigma_N = \sqrt{N + 0.75}$.

We use this to compute radial surface brightness profiles which we normalize by the counts in the central bin. For observations and energy ranges which demonstrate statistically significant extended emission we repeat the process with annuli split into quadrants aligned in the cardinal directions. This allows investigation of potential azimuthal variation in the extended emission, which would be further evidence of an origin unrelated to *Chandra* PSF spread, which is radially symmetric to first order (Allen, Jerius & Gaetz 2004).

3.4 [O III] to soft X-ray ratios

There is a well-known relationship between soft (0.5–2 keV) X-ray emission and [O III] emission, which is often found to be coincident in extent and morphology (see e.g. Bianchi, Guainazzi & Chiaberge 2006; Wang et al. 2011). The ratio itself has been found to be inversely proportional to the ionization parameter of the gas (Bianchi et al. 2006). To produce a spatially resolved image of this ratio across NGC 5972, we convert our *HST* [O III] image to energy flux units by multiplying by inverse sensitivity (*PHOTFLAM* header keyword) and the effective width of the filter. The effective width of the FR505N tunable ramp filter (centred on 5156 Å) was calculated with the

[7] http://cxc.harvard.edu/ciao/threads/prepchart/

Downloaded from https://academic.oup.com/mnras/article/526/3/4174/7288715 by Cal Polytechnic State Univ San Luis Obispo user on 29 November 2023

STSYNPHOT package to be 112.07 Å. We then smooth and reproject the *HST* image to match the angular resolution and pixel scale of the binned *Chandra* data. To create an X-ray image in units of erg cm^{-2} s^{-1} we use the output image of MERGE_OBS filtered to between 0.3 and 2 keV, with 1:1 pixel binning and multiply by the average energy of the events using DMIMGCALC. We then crop to the scale of the *HST* WFC-3, and use DMIMGCALC to calculate the ratio of the two images.

3.5 Optical spectra

3.5.1 Optical emission-line fitting

The 2D *HST* spectra have both a spatial and spectral axis, which allows investigation of the line and continuum emission at positions across the [O III] bubble. Fig. 1 shows the orientation of the STIS extraction slit along the long axis of the bubble which allows us to probe the velocities and strength of line emission at different locations across the [O III] bubble. The G750M grating, which contains the notable emission lines; Hα, [N II] λ6585, [N I] λ6529, and the [S II] λ6718/6733 doublet, shows very little continuum emission above background. The G430L grating, which is dominated by the [O III] λ5008 emission line, shows some evidence of weak continuum background. This background is low and constant across this emission line, so we fit it only as an additional additive constant during this analysis. We first shift the wavelength axis to account for the redshift of the galaxy due to the *Hubble* flow. We infer the redshift of the galaxy from the Calcium (Ca II) absorption triplet at vacuum wavelengths 8498, 8542 and 8662 Å, which is a tracer of old stellar populations (Andretta et al. 2005). We choose this feature because it is in the NIR, so it is less affected by reddening and dust absorption. We review spectra of NGC 5972 from the SDSS DR16 (Ahumada et al. 2020), with a spatial single fibre resolution of 3arcsec marginally sufficient to resolve the central region. In the spectra the Calcium triplet is clearly visible, with observed wavelengths 8752, 8798, and 8923 ($\pm$5) Å respectively, which corresponds to an average redshift of 0.0300 $\pm$ 0.0001.

We fit a single Gaussian component to each of the Hα, [N II] λ6585, and [O III] λ5008 emission lines at different spatial offsets using the *lmfit* package. The model finds the best fits and confidence intervals of the mean wavelength, FWHM, and amplitude for each line. We also fit two Gaussian components to the emission lines spatially integrated across the central 0.3 arcsec of the bubble to search for evidence of kinematically disturbed gas. We fit one dominant component to each emission line, with an additional secondary component fitted to fainter emission from kinematically offset gas.

The resultant fitted models are filtered to exclude models with extreme FWHM or very low amplitude. We also interactively exclude models that are a poor fit to the data. For each well-fitted emission line, the Doppler shift of the observed mean wavelength from its rest vacuum wavelength[8] is used to calculate the velocity of the gas relative to the central offset with the strongest [O III] flux. The FWHM of the emission lines are also calculated, which are a measure of the velocity spread from the broadening of the emission lines. Given that the [O III] bubble is extended, we assume that the STIS slit is filled, resulting in a 4 pixel resolution (Prichard, Welty & Jones 2022). This is equivalent to an FWHM of 2.2 and 11 Å for G750M and G430L gratings, respectively. At the wavelengths of Hα and [O III] the velocity resolution is therefore $\approx$100 and 640 km s^{-1}, respectively. We subtract the wavelength broadening from the best-fitting FWHMs in quadrature.

[8] http://classic.sdss.org/dr6/algorithms/linestable.html

3.5.2 Balmer decrement correction

In our data set, both the [N II] λ6585 Hα and [O III] λ5008 emission lines are very strong across the bubble, but the Hβ line is much weaker. As metal and Balmer absorption lines in the spectrum of later-type stars can partially or fully obscure the Hβ emission line, the stellar background continuum must be modelled and subtracted in order to accurately estimate the unabsorbed line flux (Liang et al. 2004; Groves, Brinchmann & Walcher 2012). To do this we use the *penalized pixel-fitting* (PPXF) package detailed in Cappellari (2017) which fits combinations of stellar templates to the spectra. We used the MILES library of stellar spectra (Falcón-Barroso et al. 2011) based on the Vazdekis et al. (2010) population models. We degraded the pixel scale of the Vazdekis templates (2.51 Å) to match the pixel scale of the G43OL grating. The spectral lines are masked during the fit, but the fitted stellar populations are used to estimate the Hβ flux absorbed by the stellar continuum.

We subtract the continuum model from the spectra and then calculate the flux in the Hβ line using *lmfit*. We also determine the flux in the Hα line, and calculate the central Balmer decrement (Hα/Hβ) assuming constant reddening across the bubble. We then used this relationship to estimate off-axis Hβ fluxes. We then produce the common diagnostic diagram known as a Baldwin, Phillips and Terlevich (BPT) diagram (Baldwin, Phillips & Terlevich 1981) used to identify the ionizing source. We calculate the [O III] λ5008/Hβ and [N II] λ6585/Hα ratios of emission-line flux and plot them to determine the ionization source across the bubble.

4 RESULTS

4.1 X-ray imaging

4.1.1 Nucleus

We report the detection of an above-background X-ray flux (0.3–8 keV) from the centre of NGC 5972. We measure a soft flux (0.5–2 keV) within a 2 arcsec region of the central engine of of $2.65 \pm 0.15 \times 10^{-14}$ erg cm^{-2} s^{-1} above background. This emission is spatially coincident with the bubble seen in the [O III] HST observations.

Fig. 3 shows the smoothed soft (0.3–2 keV) X-ray emission spatially coincident with the [O III] bubble. The false colour palette was chosen to highlight the surface brightness range across the emitting region. The *HST* [O III] contours are overlaid for comparison, with the brightest [O III] point labelled with a blue cross. The nuclear source location, shown with a black cross, is discussed in Section 5.1. Fig. 4 (left) shows the *HST* [O III] emission in green, the soft X-Ray (0.5-2 keV) in blue and the hard X-Ray(2-8 keV) in red. Purple contours in Fig. 4 also show the jet emission observed at 10 cm (3 GHz) with VLASS. Fig. 5 (centre) shows the same comparison but for the hard broad-band emission between 2 and 8 keV, smoothed with a 3 pixel Gaussian kernel. Fig. 5 (right) shows the smoothed 6–7 keV emission which is associated with the nuclear source. Counts within the asymmetry region have been removed as discussed in Section 5.1. Fig. 5 (left) isolates emission from the Ne IX 0.905 keV transition line (filtered to 0.865–0.938 keV), which has been associated with shocked emission in other sources (e.g. NGC 3933 Maksym et al. 2019; NGC 4151 Wang et al. 2011). This image is shown unsmoothed with 1/4 ACIS pixel binning.

Downloaded from https://academic.oup.com/mnras/article/526/3/4174/7288715 by Cal Polytechnic State Univ San Luis Obispo user on 29 November 2023

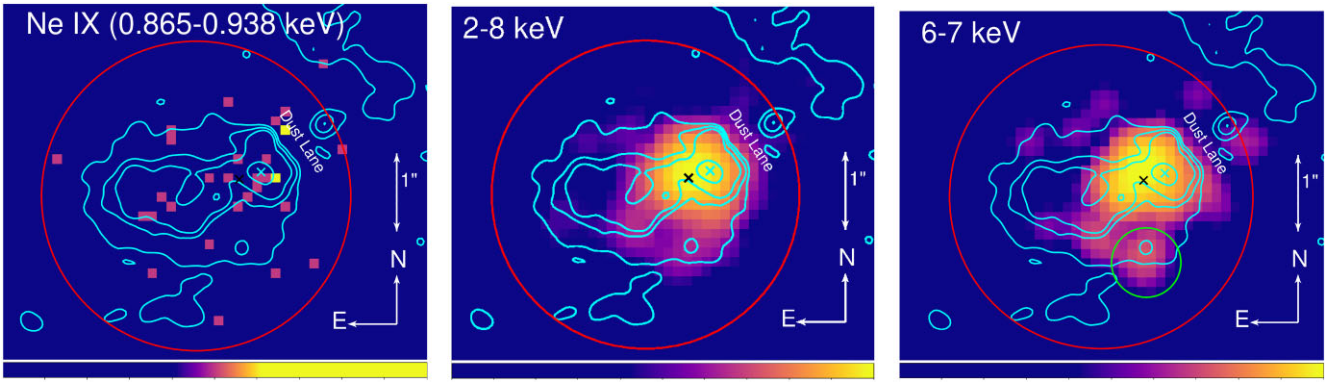

Figure 5. The Ne IX (0.865–0.938 keV, left) hard (2–8 keV, centre) and nuclear (6–7 keV, right) X-ray emission co-incident with the [O III] bubble is shown on a logarithmic colour scale. The spatially coincident *HST* [O III] observation is shown with blue contours. The data have been binned to 1/4 ACIS-s pixel size and smoothed with a 3 pixel Gaussian Kernel for the central and left figures. The Ne IX data are unsmoothed as there are a low number of counts in this narrow energy range. The red circle is the same as shown in Fig. 4 and the location of the SMBH is marked with a black cross. The green circle shows the potential point source to the south of the nucleus. The labelled dust lane was identified by Keel et al. (2015). Other figure parameters are the same as Fig. 3.

4.1.2 EELRs

We also detect an above-background soft X-ray (0.3–2 keV) flux coincident with the EELRs to the north and south of the [O III] bubble. This soft X-ray flux extends 15–20 arcsec from the central region in both the north and south directions. Fig. 4 shows the white dashed ellipses, we integrate the flux over for each EELR. We find a soft (0.5–2 keV) flux for the north (south) arm of 6.4 ± 0.7 (5.4 ± 0.7) $\times$ 10^{-15} erg cm^{-2} s^{-1} above background. Fig. 4 (left) shows the 3σ adaptively smoothed soft X-ray (0.5–2 keV) in the blue channel overlaid on the green *HST* [O III]. The red channel shows the hard (2–8 keV) emission, smoothed with a 3 pixel Gaussian. The soft X-ray emission shows the location of hot X-ray emitting gas relative to the EELR [O III] emission and is further highlighted with yellow logarithmically spaced contours. The location of the central engine and the region containing the [O III] bubble are also shown with a red cross and dashed red circle. The nuclear source location is discussed in Section 5.1. This image is smoothed to highlight the diffuse emission from the EELRs, and as a result the emission near the centre is purposefully over-exposed. Fig. 4 (right) shows the 1σ adaptively smoothed soft X-ray (0.5–2 keV) emission overlaid with contours showing the *HST* [O III] EELR emission.

We do not detect a significant hard X-ray flux coincident with either EELR, with the only exception being a potential hard X-ray point source in the north EELR. Fig. 4 shows the potential point source with a blue circle. No optical counterpart is seen in *HST* narrow-band or continuum imaging. This source is only marginally detected; we associate 6 counts between 3 and 6 keV with this source.

4.1.3 Spatial extent

Fig. 6 shows the radial surface brightness profile of the real and simulated observations for four different energy bands (0.5–1.5, 1.5–3, 3–6, and 6–7 keV) as a function of radial distance from the nuclear source location. The different observations are combined with an average weighted by exposure time, and the surface brightness is normalized by dividing each profile by the total number of counts within 0.5 arcsec of the source location. The 1σ uncertainties shown are propagated from the number of counts in each region under the Gehrels approximation. The Poisson uncertainty in the PSF simulations is negligible by comparison given the large number of simulations used. The soft emission (0.5–1.5 keV) clearly demonstrates spatial extent above the PSF up to 2.5 arcsec from the central point. The 1.5–3 keV energy band also shows potential above background emission between 1 and 1.5 arcsec from the centre. The two higher energy bands do not demonstrate any spatial extent when analysed radially. We also investigate the azimuthal dependence of the spatial extent of the soft emission. Fig. 6 shows the surface brightness profile of the soft emission as a function of radial distance for quadrants aligned in the cardinal directions. The profiles are normalized by the central number of counts in each central quadrant.

4.1.4 [O III] to soft X-ray ratio maps

For the [O III] bubble and EELRs, we compute a [O III] λ5008 flux from *HST* ACS image. For the north (south) EELR, we calculate 1.43 ± 0.06 (1.72 ± 0.07) $\times$ 10^{-13} erg cm^{-2} s^{-1} above background. For the [O III] bubble, we compute an [O III] flux of $7.27 \pm 0.45 \times 10^{-13}$ erg cm^{-2} s^{-1}.

Fig. 4 shows the ratio of [O III] λ5008 flux to soft (0.5–2 keV) X-ray flux for the regions covering the bubble and both EELRs, which we bin to the ACIS-S pixel size given the low number of counts in the EELR regions. We indicate pixels with no soft X-ray flux in black.

Combining this with our computed X-ray fluxes, we calculate average [O III]/soft X-ray flux ratios which are less sensitive to single pixel variation. For the [O III] bubble, we compute a ratio of 2.67 ± 0.23. For the north and south EELRs, we compute ratios of 24.4 ± 3.7 and 34.1 ± 5.4, respectively.

4.2 X-ray spectroscopy

4.2.1 Nucleus

The spectra are fitted to the model described in section 3.2.2 from Zhao et al. (2021), with all parameters other than the two scaling constants fixed to the authors best-fitting values. We show the absolute residuals of this model for each observation under each spectra. We first fit this model to the emission from a 0.25 arcsec region to constrain the normalization of the scaling constant for reflected emission (const$_2$), finding a best-fitting value of $1.3^{+0.6}_{-0.4}$ per cent with a reduced statistic of 0.90. For comparison, Zhao et al. (2021) found a value of 1.4 per cent, which is within error of our value.

Const$_2$ was frozen at this value, and Fig. 7 shows the fit and residuals of this model to the spectra extracted from a larger 2 arcsec

Downloaded from https://academic.oup.com/mnras/article/526/3/4174/7288715 by Cal Polytechnic State Univ San Luis Obispo user on 29 November 2023

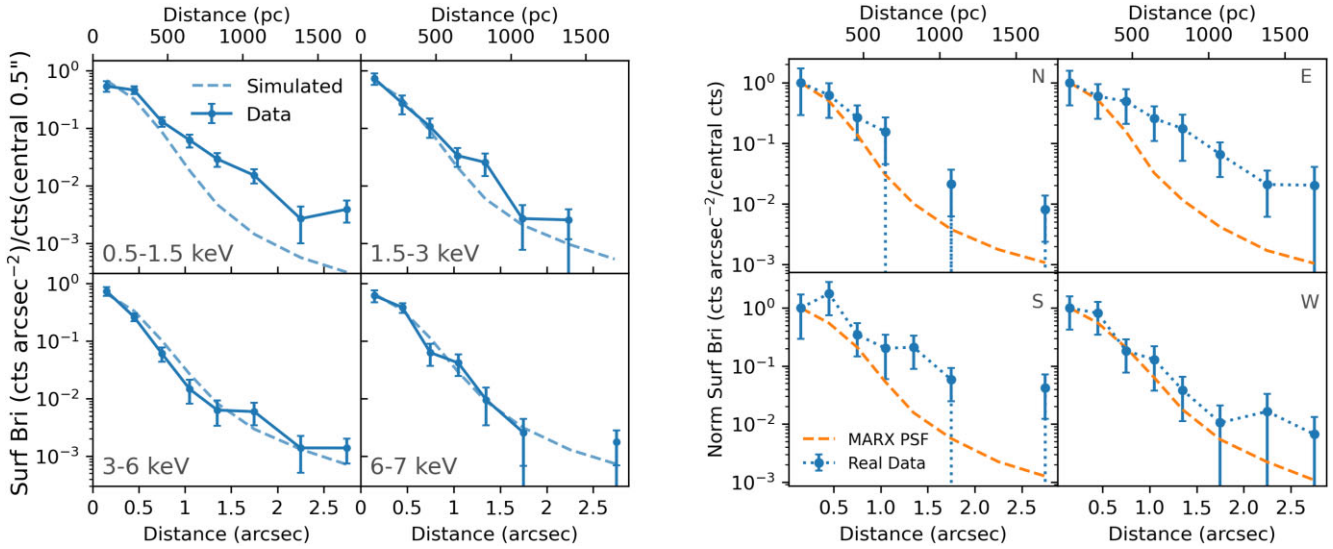

Figure 6. Left: the radial surface brightness profile of the X-ray emission in different energy bands centred on the nuclear source location in Fig. 4. The counts are extracted from concentric circular annuli. Right: the surface brightness profiles of the soft (0.5–1.5 keV) X-ray emission split into quadrants aligned with the cardinal directions. In both figures, the profile for the real observations and simulations of the *Chandra* PSF are compared, and are normalized by the total number of counts within 0.5 arcsec of the source. The uncertainties in the PSF simulations are negligible in comparison to the observed data.

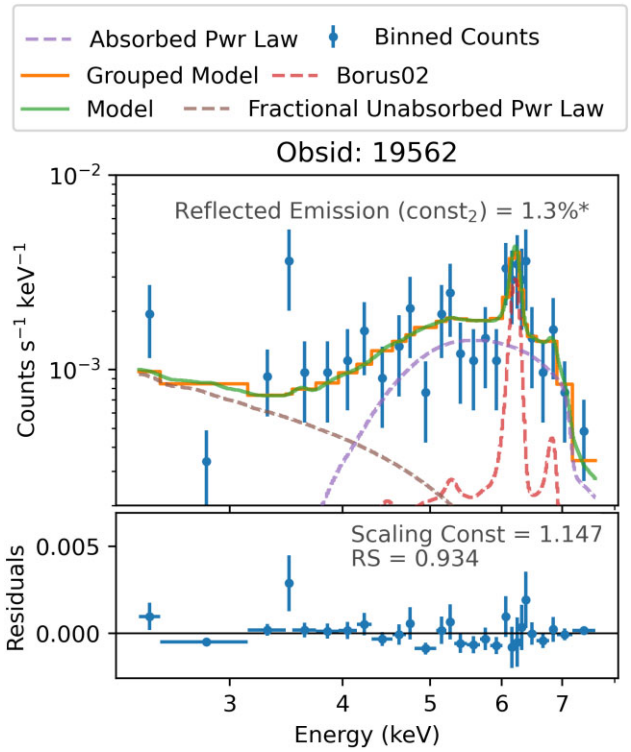

Figure 7. The hard (3–8 keV) spectra extracted from the 2 arcsec regions centred on the nuclear source location, binned to 5 counts bin^{-1}, for *Chandra* observation 19 562 of NGC 5972. Zhao et al.'s (2021) model is overlaid, with the model components shown in dashed lines. The 'Grouped Model' shown in orange, refers to the model binned to the resolution of the data. The full resolution model is also shown in green. The residuals of the model for each observation are shown underneath. The values of the scaling constants are shown, with a $*$ indicating if the component is frozen during the fitting process.

region, which we use to constrain the value of the overall scaling constant of the nuclear spectral model. The energy range is still constrained to 2.5–8 keV to exclude the soft emission. For this scaling constant (const$_1$), we calculate a value of $1.15^{+0.07}_{-0.06}$ with a reduced statistic of 0.93.

We then freeze both constants to produce a final model describing the nuclear emission above 2.5 keV. Using the same extraction region (2 arcsec circle), we now expand our allowed energy range to include soft emission between 2.5 and 0.3 keV and introduce new models to fit these spectra. Table 3 shows the results of fitting combinations of APEC and CLOUDY models to this soft emission. The columns give the model used and the physically relevant model parameters – column density and ionization parameter for the CLOUDY model and temperature and emission measure (normalization) for the APEC models. They also give the goodness-of-fit statistic, which is equivalent to the reduced χ^2 statistic, where a fit $\leq$1 indicates a good fit. Fig. 8 shows the extracted spectra across the full energy range, fitted with our best double APEC model for the soft emission. Fig. 8 shows the two fitted spectra overlaid with the best CLOUDY fit. The goodness-of-fit statistic indicates a good fit but the best-fitting column density is at the lower boundary for this model (log $N_{\rm H}$ = 19.0 cm^{-2}).

We have computed the bolometric luminosity of the AGN based on Zhao et al.'s (2021) estimate of the 2–10 keV luminosity from their X-ray spectral modelling. Zhao et al. (2021) found $6.17^{+1.07}_{-1.15} \times 10^{42}$ erg s^{-1} for the 2–10 keV luminosity based on the same spectral model. Accounting for a bolometric correction factor of 12^{+8}_{-3} taken from Netzer (2019), we find a bolometric luminosity of $L_{\rm bol} = 7.5^{+5.2}_{-2.3} \times 10^{43}$ erg s^{-1}. The bolometric correction factor is not well constrained, increasing the uncertainty in our luminosity estimate. Our bolometric luminosity estimate is consistent with the upper limit given by Keel et al. (2017) of $<1.7 \times 10^{44}$ erg s^{-1} based on *WISE* mid-IR observations. Finlez et al. (2022) find a current bolometric luminosity of 2.0×10^{44} erg s^{-1} based on Gemini Integral Field Unit (IFU) observations.

Downloaded from https://academic.oup.com/mnras/article/526/3/4174/7288715 by Cal Polytechnic State Univ San Luis Obispo user on 29 November 2023

Table 3. Table contains best-fitting model parameters for X-ray spectra extracted from the nuclear bubble, north and south EELR regions in NGC 5972. The first column gives the spectra model fitted between 0.3 and 2.5 keV, with the second and third columns giving the best-fitting parameters of that model. All models were also multiplied by a fixed *phabs* component representing Galactic absorption. The last column gives the goodness of fit in the form of the reduced statistic calculated for each model. A star next to the reduced statistic indicates that one or more of the best-fitting parameters has reached a limit in the parameter space. Where possible uncertainty bounds are indicated on model parameters, but a ±u indicates a parameter with unconstrained uncertainty.

Region	Model	Best-fitting parameters (Model 1)	Best-fitting parameters (Model 2)	Reduced statistic
Nuclear bubble	CLOUDY	$\log N_{\rm H} = 19.0^{+u}_{-u}$ cm^{-2}, $U = 0.32^{+u}_{-u}$		0.99∗
	APEC	$kT = 0.246^{+0.04}_{-0.05}$ keV, norm $= 2.4^{+1.6}_{-0.7} \times 10^{-5}$		1.06
	APEC + CLOUDY	$kT = 0.04^{+0.09}_{-0.02}$ keV, norm $= 0.6^{+21}_{-0.6}$	$\log N_{\rm H} = 19.4^{+u}_{-u}$ cm^{-2}, $U = 0.48^{+0.23}_{-0.30}$	0.99
	APEC$_1$ + APEC$_2$	$kT = 0.80^{+0.09}_{-0.12}$ keV, norm $= 4.8^{+1.8}_{-1.4} \times 10^{-6}$	$kT = 0.10^{0.06}_{-0.08}$ keV, norm $= 4.2^{+u}_{-3.7} \times 10^{-4}$	0.98
	CLOUDY$_1$ + CLOUDY$_2$	$\log N_{\rm H} = 19.0^{+u}_{-u}$ cm^{-2}, $U = 0.32^{+u}_{-u}$	$\log N_{\rm H} = 20.16^{+u}_{-u}$ cm^{-2}, $U = 0.007^{+u}_{-u}$	1.02∗
North arm	CLOUDY	$\log N_{\rm H} = 22.7^{+0.2}_{-0.2}$ cm^{-2}, $U = 1.2^{+0.3}_{-0.3}$		0.61
	APEC	$kT = 3.4^{+1.2}_{-1.2}$ keV, norm $= 9.9^{+2.0}_{-2.0} \times 10^{-6}$		1.38
	APEC + CLOUDY	$kT = 0.012^{+u}_{-u}$ keV, norm $= 0.069^{+0.06}_{-0.06}$	$\log N_{\rm H} = 1.2^{+0.3}_{-0.3}$ cm^{-2}, $U = 22.8^{+0.4}_{-0.4}$	0.74
	APEC$_1$ + APEC$_2$	$kT = 3.4^{+u}_{-u}$ keV, norm $= 9.8^{+u}_{-u} \times 10^{-6}$	$kT = 0.008^{+u}_{-u}$ keV, norm $= 8^{+u}_{-u} \times 10^{-4}$	1.65∗
	CLOUDY$_1$ + CLOUDY$_2$	$\log N_{\rm H} = 22.8^{+u}_{-u}$ cm^{-2}, $U = 1.2^{+u}_{-u}$	$\log N_{\rm H} = 19.6^{+u}_{-u}$ cm^{-2}, $U = 0.07^{+u}_{-u}$	0.83
South arm	CLOUDY	$\log N_{\rm H} = 19^{+u}_{-u}$ cm^{-2}, $U = 1^{+u}_{-u}$		1.43∗
	APEC	$kT = 0.63^{+0.12}_{-0.12}$ keV, norm $= 4.5^{+1}_{-1} \times 10^{-6}$		1.3

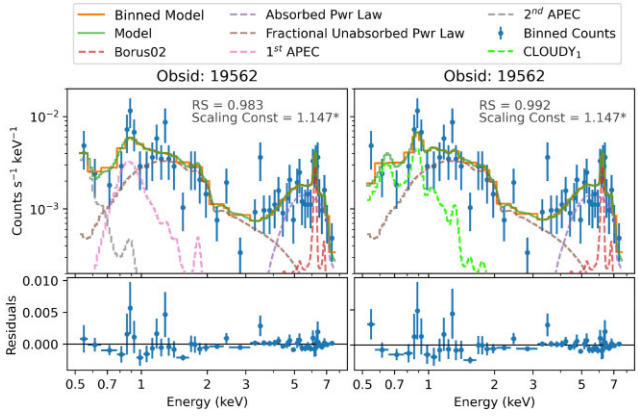

Figure 8. The 0.3–8 keV X-ray spectra extracted from a 2 arcsec region centred on the nuclear source location for ObsID 19562, binned to 5 counts bin^{-1}, for two of the *Chandra* observations of NGC 5972. On the right plot, the best-fitting double APEC model is shown with grey and pink dashed lines, and on the left plot, the best-fitting CLOUDY model is shown with a green dashed line. Zhao et al.'s (2021) model is included for the harder emission. The residuals of the model for each observation are shown underneath. The goodness-of-fit statistic, overall scaling constant are shown for both fits.

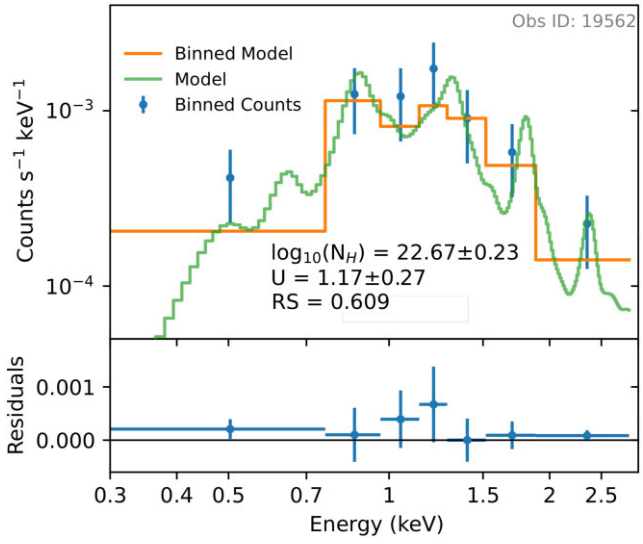

Figure 9. This figure shows the spectra extracted from the north EELR region, which is indicated by dashed white ellipse in Fig. 4 for ObsID 19562. The spectra are binned to 5 counts bin^{-1} and the error bars indicate the 1σ uncertainty under the Gehrels approximation. The best-fitting photoionization (CLOUDY) model is overlaid, both at its native resolution and binned to the same resolution as the spectra. The reduced statistic indicating the goodness of fit of the model, as well as the best-fitting parameters and their uncertainties are shown. The residuals of the model to each binned point are also shown in the lower plots.

4.2.2 EELRs

Table 3 shows the results of fits of combinations of thermal (APEC) and photo-ionization (CLOUDY) models fitted to spectra extracted from the elliptical regions covering the north and south EELRs. The best-fitting parameters and goodness-of-fit statistic are given. Fig. 9 shows the best-fitting model and corresponding residuals for the spectra extracted from the north EELR. The best model is a single CLOUDY multiplied by an absorbing *phabs* model tied to the Galactic absorption from the Milky Way. This model is not a good fit to the spectra from the south EELR.

4.3 STIS spectroscopy

4.3.1 Emission-line profiles

Fig. 10 shows the spectra extracted from the 2D STIS spectra along the central row, which is defined as the row with the strongest line emission. In pixel coordinates, this corresponds to row $y = 626$ and 627 for the G750M and G430L observations, respectively. The spectra are shown uncorrected for their redshift, but the theoretical wavelength of common emission lines are overlaid for the Ca-triplet derived redshift ($z = 0.0300$). The vacuum wavelengths are taken from the SDSS table.[9] The theoretical wavelengths show a systematic offset from the emission lines shown because of the relative velocity difference of the central region relative to the derived systemic velocity of the system. For the G430L spectra, where we fitted the stellar continuum to find the unabsorbed Hβ flux using PPXF, the stellar continuum subtracted spectra is also shown.

[9] http://classic.sdss.org/dr6/algorithms/linestable.html

Downloaded from https://academic.oup.com/mnras/article/526/3/4174/7288715 by Cal Polytechnic State Univ San Luis Obispo user on 29 November 2023

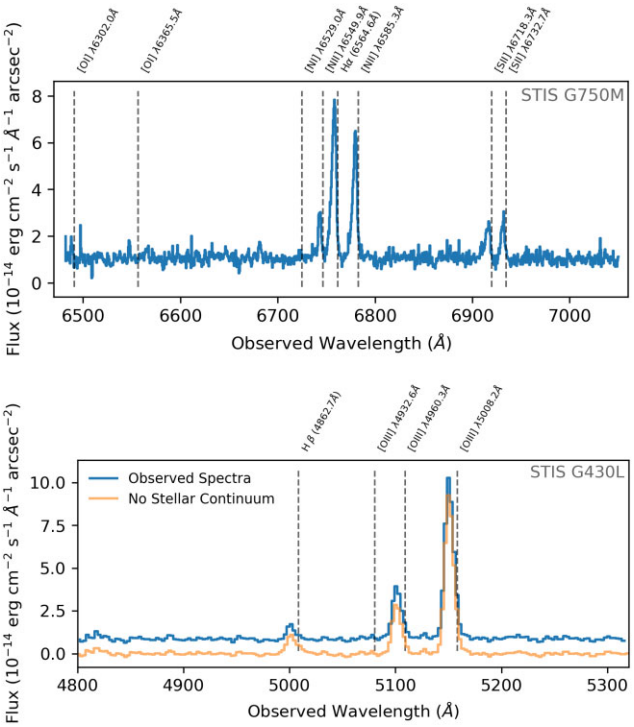

Figure 10. Top (bottom): STIS G750M (G430L) spectra of the nuclear bubble, summed across the 0.5 arcsec region surrounding the central row of the 2D spectra. The observed wavelength is shown, as well as the wavelengths and names of common emission lines. For the G430L spectra, both the observed spectra and the stellar continuum subtracted spectra from PPXF are shown for comparison.

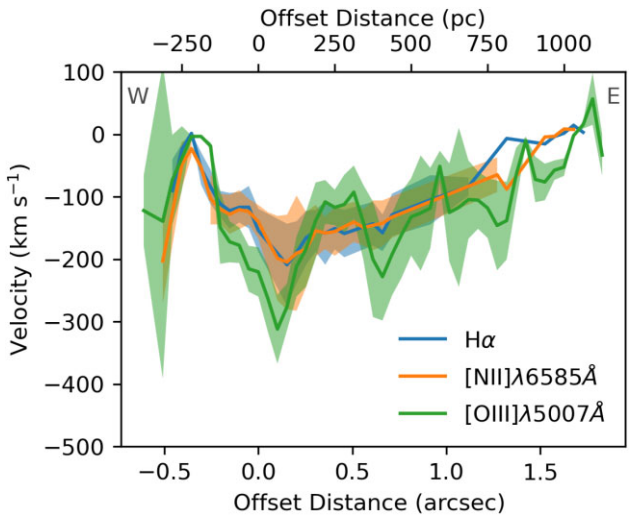

Figure 11. The radial velocity profile of the gas across the bubble computed from the Doppler shift of the bright [O III], Hα, and [N II] emission lines relative to their strongest points. The confidence intervals shown are propagated from the uncertainty in the Gaussian fitted to each emission line. The on the sky orientation of the extracted velocity profile is indicated by the cardinal directions in the upper right/left corners.

4.3.2 *Kinematics*

Fig. 11 shows the computed radial velocity of the gas within the bubble as a function of offset position. The radial velocity was computed from the Doppler shift of the Hα, [N II], and [O III] emission lines relative to their rest wavelengths. The offset position (x-axis) was determined relative to the spectrum with the highest [O III] line flux, which we have assumed to correspond to the brightest [O III] region in the *HST* imaging.

The Hα emission line spatially integrated across the inner 0.2 arcsec of the bubble was best fit with a double Gaussian profile, with a secondary component offset by 4 Å contributing to a faint 'wing' with 5 per cent of the flux of the primary line. This corresponds to a velocity offset of 210 km s^{-1}. The addition of a second Gaussian to the fit of the spatially [N II] and [O III] emission lines did not improve the fit.

After subtraction of the instrumental broadening from the best-fitting FWHM of the emission lines, we see no evidence of resolved velocity broadening above the resolution of the filled slit across the majority of the [O III] structure, particularly in the lower resolution G430L filter. This places an upper limit on the possible [O III] velocity broadening of $\approx$ 640 km s^{-1}, which is the resolution of the G430L grating with a filled slit at the wavelength of the [O III] emission. In the G750M, we see peak velocity FWHMs of up to $\approx$300 km s^{-1}, centred on the region of brightest [O III] emission. Further from the centre, we see no velocity broadening above the $\approx$ 100 km s^{-1} resolution of the G750M grating with a filled slit at the wavelength of Hα.

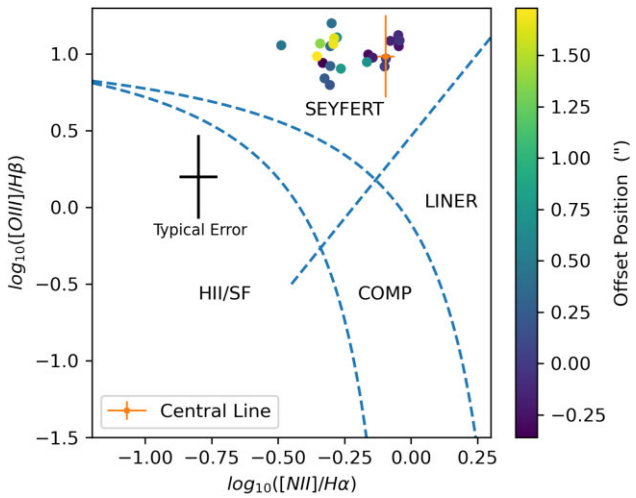

Figure 12. BPT diagram (Baldwin et al. 1981) showing the ratios of diagnostic lines as a function of offset position across the [O III] bubble. The ratio of these lines indicates the ionizing source, which are labelled in black and separated by the shaded blue lines Kauffmann et al. (2003). See Section 3.5.2 for more details. The offset position is indicated by the colour bar on the right side of the plot. For comparison, the Hβ line strength at the central position is shown in orange.

4.3.3 *BPT mapping*

From our fitting of the optical continuum using PPXF, we find a best fit with the contributions from three stellar populations of distinct ages; a dominant component of old stars (age approximately 15 Gyr) and two young stellar populations of ages 0.4 and 0.06 Gyr. Subtracting this model for the stellar continuum and fitting the central Hα and Hβ lines, we find a Balmer decrement of 3.6 $\pm$ 2.2. We use this Balmer decrement as a proxy to estimate Hβ fluxes across the bubble for the BPT diagram, assuming constant reddening. Fig. 12 shows the BPT diagnostic diagram (Baldwin et al. 1981) for different offset regions across the [O III] bubble. The offset of a

Downloaded from https://academic.oup.com/mnras/article/526/3/4174/7288715 by Cal Polytechnic State Univ San Luis Obispo user on 29 November 2023

particular point from the central position (highest flux [O III] offset) is shown by the marker colour. As the Hβ flux for offsets across the bubble is inferred from the Hα/Hβ Balmer decrement at the central offset, this point is also plotted in orange for comparison. The average uncertainty for both ratios is shown. There is no clear trend across the [O III] bubble in either of the ratios. All the emission from regions within the [O III] bubble is consistent with emission from an AGN (Seyfert) source. These results agree with Finlez et al. (2022) who find a stellar population within the bubble with an age of approximately 12 Gyr. The authors also find that the bubble and EELRs are consistent with ionization from AGN continuum emission.

5 DISCUSSION

5.1 Nuclear source location and [O III] mismatch

The neutral and ionized iron lines (Fe Kα, Fe XXV and Fe XXVI) emit 6–7 keV radiation from the outer accretion disc and the inner obscuring torus of the SMBH, detectable as point-like emission given the angular scale $\sim$600 pc arcsec^{-1} and the 0.1−0.2 arcsec angular resolution. The centroid then serves as a signature of the central engine (e.g. Maksym et al. 2017). The exact location of the AGN is important for spectroscopic and surface brightness profile analysis. In Fig. 5, an almost unresolved point source appears about 1 arcsec to the south of the central region, which is most likely an artefact of PSF asymmetry in the *Chandra* PSF at small scales (see Kashyap 2010) is the most likely source of this anomalous point source. We remove some of the excess counts within the asymmetry region based on the PSF simulations to find the final uncontaminated point source location. We find that while there is still an excess grouping of counts above the predicted level, it is not statistically significant enough to confirm a second X-Ray source. The nuclear source location determined by this method (RA: 15:38:54.1575, Dec. +17:01:34.449) is used to generate the simulated PSF, as the central point for computing the surface brightness gradient, and is shown by the black cross in Fig. 3. The brightest [O III] emission is located at RA 15:38:54.1379, Dec. +17:01:34.543 and is shown by the green cross in Fig. 3. The distance between the X-ray source location and the brightest [O III] point is 0.3 $\pm$ 0.2 arcsec. The model used in Zhao et al. (2021) constrains the torus and inclination angles of the AGN as 32° and 26°, respectively, suggesting the bi-cone could be aligned with the plane of the sky. If so, the Fe Kα emission would be absorbed by the Compton-thick torus but [O III] emission from the more distant NLR would still be observed. Offset between the X-ray and AGN centroids may be because the inner NLR is likely to be clumpy with regions of high dust extinction, leading to non-uniform absorption.

5.2 Spectra and morphology of the bubble

We have tested models for the soft X-ray spectra for both a thermally ionized plasma (the APEC model) and for photoionization by an AGN (the CLOUDY model), as well as combinations of these models. We find that the soft X-ray spectrum is statistically consistent with both a multicomponent thermally ionized plasma (two APEC components) as well as photoionization from an unobscured AGN continuum.

When we look at the double APEC fit, we see some correlation in the residuals, with an excess near 0.9 keV that can potentially be attributed to Ne IX emission, but may also have contributions from the [Fe XVIII], [Fe XIX], and [Ni XIX] lines with similar energies. Fig. 5 shows the Ne IX emission from the bubble, which in other systems is indicative of shocked emission (e.g. NGC 3933, Maksym et al. 2019; NGC 4151, Wang et al. 2011). The bulk of the soft emission is best fitted by a single APEC model with a temperature of 0.80 keV, with the other component modelling the very soft 0.5 keV excess at a poorly constrained temperature of $\approx$0.1 keV.

The spectrum is also statistically well fitted by the single CLOUDY model, but we see significant correlated residuals suggesting that not all the spectral features are modelled correctly, including notably the soft excess at 0.5 keV. Multiple CLOUDY components with different column densities and ionization parameters do not improve the fit or the residuals, although given the extent of the region ($\approx$2.5 kpc diameter), it is likely that there is variation of both of these parameters. Furthermore the column density, we find is at the lower bound allowed by the tabulated CLOUDY model (log $N_{\rm H} = 19.0\,{\rm cm}^{-2}$). We were unable to compute a confidence interval for either parameter, so the upper limit is unconstrained. The medium could be clumpy, with knots of high column density, but the best-fitting column density is likely an underestimate of the true average column density across this region. The best-fitting column density being at the lower limit of the allowed parameter space further suggests that despite a statistically robust fit, this CLOUDY model may not be a good physical description of this system.

Overall, for the reasons discussed above we prefer the model based on the multicomponent thermally ionized plasma rather than direct photoionization by the AGN, but we cannot exclude either scenario. We also considered a model combining both components, where the bulk of the emission was fit by the CLOUDY model and the soft excess was fit by an APEC model, which was also statistically well fitted to the data. One comparison that can be made is to extended narrow-line regions (ENLRS) in other systems, which display the same signatures of AGN-influence across kpc scales. X-ray studies of sub-kpc ENLRS (e.g. Paggi et al. 2012; Bogdán et al. 2017; Fabbiano et al. 2018) have shown that the gas populations within ENLRs are multiphase, with roles for both photoionized and collisionally ionized plasma. For NGC 5972 contributions from both components may therefore be needed to fully explain the ENLR emission. A deeper *Chandra* observation (a few hundred ks) would provide better signal to noise for spectroscopy and allow us to better differentiate between these two hypotheses. Additionally a longer observation would allow us to de-convolve the effects of the PSF and make better comparisons to the small-scale [O III] structure.

The soft X-ray emission coincident with the [O III] bubble shows a broadly similar morphology to the [O III] structure, with the same spatial extent. We see soft X-ray emission from the region NW of the nucleus containing a dust lane, which may suggest that [O III] emission is selectively obscured, while soft X-ray emission is not. The surface brightness profiles indicate that there is extended soft (0.5–1.5 keV) X-ray emission out to 2.5 arcsec (1500 pc), which is preferentially extended along the long axis of the [O III] bubble. The BPT maps suggests that the emission observed is consistent with photoionization by an AGN-like source. Whilst the ratios of [O III]/Hβ shown in the BPT diagram are compatible with the best-fitting ionization parameter calculated from the fits to the soft X-ray spectra (Groves & Allen 2010), this emission-line diagnostic is less sensitive to the ionization parameter in the regime where $\log_{10} U \geq 0$. Other emission-line diagnostics would be required to provide stronger evidence for the measured ionization parameter (see e.g. Storchi-Bergmann et al. 1998; Groves, Dopita & Sutherland 2004; Levesque & Richardson 2013; Richardson et al. 2014).

One possibility is that the [O III] bubble and associated extended soft X-ray emission is a signature of hot gas ablated from the inner

Downloaded from https://academic.oup.com/mnras/article/526/3/4174/7288715 by Cal Polytechnic State Univ San Luis Obispo user on 29 November 2023

disc venting through a gap in the torus. An outflow directed into the plane of the galaxy could encounter dense molecular clouds, which may be shocked but not efficiently entrained by the outflow. The outflow could then continue to move along the most efficient path, likely to be out of the plane of the galaxy away from high-density obstacles, similar to a vent (Mukherjee et al. 2018). Such vented outflows may carry entrained gas, or even shock lower density material outside the plane, and those shocks could produce X-rays and [O III] gas such as we see in NGC 5972. A comparable example may be found in IC 5063, described in Maksym et al. (2021), which shows morphological similarities to NGC 5972. The bubble in NGC 5972 may also be similar to the AGN studied in Mingozzi et al. (2019), who use Multi Unit Spectroscopic Explorer (MUSE) IFU data to look at the central regions of nearby Seyfert galaxies with prominent (bi-)conical outflows. They find evidence for two distinct populations of ionized clouds with distinct differences in ionization parameter and emission-line ratios, and suggest low-ionization regions are found perpendicular to the cones due to a filtering of the AGN radiation.

5.3 Pressure and density

Whilst we cannot exclude the photoionization model, the reduced statistic indicates that the soft emission is well fitted by the double APEC model. Based on this model, we can estimate a number of other properties for the gas.

The double APEC model represents a multicomponent thermally ionized plasma. If we assume the gas is dominated by a collisional outflow we can estimate physical parameters of the gas within the bubble. From the best-fitting emission measures (normalization) and temperatures of the double APEC model, we can derive an average thermal pressure by this equation from Paggi et al. (2012):

$$\mathrm{EM} = \frac{10^{-14}}{4\pi\, D_A^2 (1+z)^2} \int n_e n_H \mathrm{d}V, \qquad (2)$$

where D_A is the angular distance, z is the redshift, and n_e and n_H refer to the number densities of the electrons and hydrogen atoms respectively. We assume an ideal proton-electron gas (i.e $\mathrm{n}_e = \mathrm{n}_\mathrm{H}$) and the pressure–temperature relation of $p_\mathrm{th} = 2 n_e k T$, where p_th is the thermal pressure, T is the gas temperature, and k is the Boltzmann constant. We also assume the density and temperature of the gas is approximately constant across the bubble.

We measure the on-sky size of the bubble from the [O III] *HST* image, assuming a similar size for the coincident X-ray gas population. As is done in Maksym et al. (2019), we model the shape of the bubble as an ellipsoid, with the z-axis size estimated as the shorter axis of the ellipsoid. We calculate all spatially dependent parameters (e.g. kinetic power P_kin and crossing time t_cross) relative to the longest axis of the ellipsoid. The major semi-axes of the bubble are estimated as 1.40 arcsec × 0.95 arcsec × 0.95 arcsec (±10 per cent) which is equivalent to (850 ± 90 pc × 590 ± 60 pc × 590 ± 60 pc). This gives a volume of 1.2 ± 0.2 kpc^3. For X-ray emitting plasma, we expect a density of around 1 cm^{-3} and thermal pressure of $p_\mathrm{th} \approx 10^{-10}$ dyne cm^{-2} (Paggi et al. 2012).

5.4 Feedback effects from X-ray spectroscopy

We follow the method used in Paggi et al. (2012), Sartori et al. (2016), and Maksym et al. (2019) to estimate the interaction between the AGN and the ISM within the bubble. The results of the following calculations are shown in Table 4. Many of the equations and principles are adapted from the study of bubbles/cavities within dense galaxy clusters (e.g. Bîrzan et al. 2004; McNamara & Nulsen 2012; Vantyghem et al. 2014). Using the estimated volume V and thermal pressure p_th, we can calculate an average thermal energy budget using $E_\mathrm{th} = \frac{\gamma}{\gamma-1} p_\mathrm{th} V$. the heat capacity ratio, γ, of a non-relativistic monoatomic gas is 5/3. We calculate a shock velocity for the gas using: $v_\mathrm{shock} \approx 100\,\mathrm{km\ s^{-1}} \times (kT/0.013\,\mathrm{keV})^{0.5}$ per Raga, Noriega-Crespo & Velázquez (2002), where kT is the energy of the gas in KeV. The crossing time is then simply the length of the relevant axis of the ellipsoid divided by the shock velocity.

We can calculate a sound speed $\mathrm{c_s}$ from $c_\mathrm{s} = (\gamma kT/\mu m_\mathrm{H})^{0.5}$ (Bîrzan et al. 2004) where μ=0.62, and $\gamma = 5/3$. μ is a scaling factor for the average particle mass taken from Bîrzan et al. (2004).

We use the best-fitting APEC models to calculate an unabsorbed and unconvolved energy flux for each component using the SHERPA tool *calc_energy_flux*, the results of which are shown in Table 4. The corresponding thermal luminosities are calculated by integrating the flux over 4π steradians at the luminosity distance of $d = 133 \pm 9$ Mpc. The cooling time is then simply the total thermal energy budget divided by this luminosity. For the hotter component ($\mathrm{APEC_1}$), the cooling time is 20–30× longer than the crossing time, suggesting no extra heating source is required. For the cooler component, the crossing time is longer than the cooling time, suggesting an extra heating component may be needed, but both of these time estimates are not well-constrained.

We can calculate a lower limit on the fraction of kinetic power heating the ISM as $L_\mathrm{K} \geq E_\mathrm{th}/\mathrm{t_{cross}}$ (Paggi et al. 2012). We can then compare these to our calculated bolometric luminosity to estimate the efficiency of the feedback processes.

The crossing time of the bubble for either component is much longer than the light travel time (about 5 kyr), suggesting the bubble is much older than the current period of variability and not related to a recent shock or outflow. The ratio of kinetic power to bolometric luminosity of $0.8^{+0.3}_{-0.2}$ per cent from the dominant APEC component is indicative that there is efficient feedback that could drive hot gas outflow and clear out the gas over large time-scales, as Hopkins & Elvis (2009) suggest a lower threshold of $P_\mathrm{kin}/L_\mathrm{bol} > 0.5$ per cent for a two-stage feedback model. There is no evidence of feedback efficient enough to directly entrain the ISM.

Table 4. The results of the calculations based on the best-fitting APEC models detailed in Section 5.3. Units are given next to the parameter name where appropriate. The upper and lower bounds or 1σ uncertainty are given where they have been computed.

Parameter	$\mathrm{APEC_1}$ model	$\mathrm{APEC_2}$ model
kT (keV)	$0.80^{+0.09}_{-0.11}$	$0.10^{+0.06}_{-0.08}$
EM	$5.0^{+1.8}_{-1.4} \times 10^{-6}$	$4.2^{+\mathrm{u}}_{-3.7} \times 10^{-4}$
APEC flux (erg cm^{-2} s^{-1})	$1.5 \pm 0.6 \times 10^{-14}$	$1.6 \pm 1 \times 10^{-13}$
APEC luminosity (erg s^{-1})	$2.9 \pm 1.2 \times 10^{40}$	$3.1 \pm 2.1 \times 10^{41}$
Electron density (cm^{-3})	0.17 ± 0.04	$1.6^{+\mathrm{u}}_{-0.7}$
Pressure (dyne cm^{-2})	$4.2^{+1.2}_{-1.1} \times 10^{-10}$	$4.8^{+\mathrm{u}}_{-4.4} \times 10^{-10}$
Total energy budget (erg)	$3.8^{+1.2}_{-1.2} \times 10^{55}$	$4.3^{+\mathrm{u}}_{-4} \times 10^{55}$
Shock velocity (km s^{-1})	780^{+50}_{-50}	270^{+80}_{-110}
Sound speed (km s^{-1})	450^{+30}_{-30}	160^{+50}_{-60}
Cooling time (Myr)	42^{+14}_{-13}	$4.4^{+\mathrm{u}}_{-4}$
Crossing time (Myr)	2.1 ± 0.3	$6.1^{+1.9}_{-2.5}$
Kinetic power (erg s^{-1})	$\geq 5.7 \pm 1.9 \times 10^{41}$	$\geq 2.2^{+\mathrm{u}}_{-2} \times 10^{41}$
$P_\mathrm{kin}/\mathrm{L_{bol}}$	$\geq 0.8^{+0.3}_{-0.2}$ per cent	$\geq 0.30^{+\mathrm{u}}_{-0.2}$ per cent

Downloaded from https://academic.oup.com/mnras/article/526/3/4174/7288715 by Cal Polytechnic State Univ San Luis Obispo user on 29 November 2023

Given the decrease in L_{bol} on time-scales much shorter than both the crossing time and the cooling time of either of our gas components, our estimate of the kinetic power may be based on emission from gas which has not had time to respond to the decreasing bolometric luminosity. This may lead to overestimates of the 'instantaneous' feedback efficiency in AGN which show large luminosity variations. Observations with better angular resolution and effective area with a proposed mission like LYNX (Gaskin et al. 2018) are required to better resolve the full effects of feedback within the bubble.

5.5 Spectra and morphology of EELRs

The soft X-ray spectra of the north EELR are best fitted by the CLOUDY model, meaning that as we expect the gas is consistent with ionization by AGN emission. The best-fitting column density of 22.7 ± 0.2 cm^{-2} and ionization parameter $U = 1.2 \pm 0.3$ suggest we are observing a moderately obscured and highly photoionized gas. Given the inferred geometry of the system (e.g. in Keel et al. 2015; Zhao et al. 2021), the EELRs are located within the bi-cone of the AGN with a large opening angle into the plane of the sky and directly photoionized by the AGN emission. The source of the obscuration is not certain, but the X-ray gas may be screened by the large amount of [O III] gas, particularly at larger projected distances. There is also a potential role for dust obscuration given that Keel et al. (2017) observe a dust lane to the NE of the bubble.

It is possible that there are large variations in column density and ionization across the EELR given the large variation in projected extent from the AGN. In Fig. 4, the soft X-ray emission from the north EELR shows a similar surface brightness over a large range of projected extent from the EELR ($\approx$ 15 arcsec or 9 kpc). Irrespective of the recent variability of the AGN, if the column density was constant across this region we would expect a non-uniform intrinsic X-ray luminosity as we do not observe a brightness gradient. For a uniform point source, we would expect an SB $\propto 1/r^2$ gradient in brightness with increasing distance from the AGN.

The 3σ smoothed soft X-ray emission in Fig. 4 appears somewhat diffuse, potentially as a consequence of smoothing relatively few counts across a larger area. However at low significance, the 1σ adaptively smoothed soft X-ray image shows regions of higher emission, potentially correlated with the [O III] EELR emission. The [O III] emission is clumpy, with knots of high surface brightness emission, so if the X-ray emitting gas is co-spatial it is possible that it is also somewhat clumpy, with variable column density and unresolved knots and cavities. It is generally coincident with the [O III] gas, potentially suggesting a multiphase medium, however there are regions with soft X-ray emission which display no co-spatial [O III] emission (e.g. isolated contour to NW of north EELR, extended contour to the E of the north EELR). In the south EELR, the soft X-ray appears to follow the curved [O III] tail but with the X-ray peak at a larger projected distance, which is suggestive of a weak shock inducing soft X-ray emission. The isolated contour west of the north EELR is aligned with the jet orientation inferred from the VLASS observation, and so it may be unrelated to the EELR but a signature of a jet-induced shock producing soft X-rays.

Fabbiano et al. (2019) have shown that soft X-ray emission can be a useful diagnostic of X-ray emission over longer time-scales than [O III] emission (on the order 10^7 yr). A deeper *Chandra* observation would allow us to constrain the AGN variability over Myr time-scales, averaging over individual duty cycles to probe the overall accretion rate of the AGN. Given the spacing of the radio lobes (330 kpc), shown in Fig. 2, and the current (67° misalignment of the jets relative to the lobes is suggestive that there has been significant jet activity and variation on similar time-scales. The radio jet within the north EELR is at a radial distance of approximately 15 arcsec (9 kpc), without considering possible projection effects which would increase this distance. To calculate an order of magnitude minimum jet age, we assume a jet velocity of anywhere between 0.05–0.9c (Livio 1999), giving a minimum jet age of 30–600 kyr. This estimate is the same order of magnitude as the current observed variability, suggesting there may be a relationship between the jet and the AGN state change.

The long axis of the [O III] bubble is also misaligned with the other features. Similar misalignments between jets and lobes are seen in 're-started' AGN', where the jets undergo a dramatic shift in orientation, but the radio lobes relics from the previous emission are still observed (e.g. Hodges-Kluck et al. 2010; Saripalli et al. 2013). We see no evidence for a radio lobe associated with the new jet. The jet shift may be due to significant interaction or merger, which we do see other evidence for in this galaxy, or evidence of a binary black hole (e.g. Merritt & Ekers 2002; Campanelli et al. 2007). We speculate that the overall misalignment could be explained by the presence of a binary SMBH system, which could support a more complex system of outflows, jets, and ionization cones (e.g. Rubinur et al. 2017). Such double SMBH have been observed (e.g. Komossa et al. 2003; Zhou et al. 2004; Koss et al. 2016; Voggel et al. 2022), but if both are actively accreting (dual AGN) they are often associated with double-peaked emission lines that are not resolved here (Shen & Loeb 2010). The existence of double-peaked lines would also depend on the dynamics of the binary system. Double-peaked lines can also sometimes be caused by the rapid rotation of the BLR without the presence of a binary (Eracleous, Lewis & Flohic 2009). A dual AGN could also explain our difficulty in constraining the centroid because two active SMBHs emitting hard nuclear spectra could appear as two almost-unresolved sources given the subarcsecond resolution of the ACIS detector. Higher resolution radio observations to better resolve the bubble and jets would provide greater insight into the cause of the misalignment.

Spectroscopy of extended soft X-ray emission in other AGN tend to be best fitted by some combination of photoionization and thermal components (e.g. Wang et al. 2011; Paggi et al. 2012; Fabbiano et al. 2018). In our case, we do not find that the introduction of a thermal component improves the fit and is minimized by the fitting algorithm. The poor fitting of any model to the south arm is not necessarily suggestive that it is not well fitted by a photoionized or thermal model. The south arm region contains fewer counts than the north region. Averaging over a large-scale, complex system with low X-ray surface brightness means our spectra are poorly resolved and may not be well approximated by our simple models.

5.6 [O III] to soft X-ray ratios

Bianchi et al. (2006) showed that the ratio of [O III] to soft X-ray (0.5–2 keV) flux is inversely proportional to the ionization parameter U if both the X-ray and [O III] emission are produced by the same photoionized medium. We can make comparisons to ratios observed in NGC 4151 and HV. For clouds within NGC 4151, Wang et al. (2009, 2011) find ratios of $\sim$10–15, independent of the cloud distance from the nucleus. They also find outliers with ratios as high as 100, implying lower ionization parameters, which they suggest may be due to intervening absorption. A constant ratio implies a constant ionization parameter, which requires a density $\propto r^{-2}$ as expected for the NLR or a nuclear wind.

Downloaded from https://academic.oup.com/mnras/article/526/3/4174/7288715 by Cal Polytechnic State Univ San Luis Obispo user on 29 November 2023

For HV, Fabbiano et al. (2019) find a [O III] to soft X-ray ratio of ∼200, which is considerably higher than our values for either EELR. This suggests that NGC 5972 is more highly ionized, which is backed up by the ionization parameter of $U = 1.2$ inferred from the spectral fitting. For the [O III] bubble, where we find a ratio of ∼3, this is comparable to the ratios, Wang et al. (2011) find within the radio jets. This high ratio may indicate very efficient X-ray photo-ionization, or that some [O III] flux is obscured.

Analysis of the ratio map are limited by the low X-ray surface brightness, but we do find that in the EELR the highest ratios are found in the gas nearest to the AGN, suggesting that the regions of high [O III] flux have lower soft X-ray emission, despite the proximity to the AGN. One hypothesis is that this [O III] emission comes from dense regions which screen the X-ray emitting gas, preventing photoionization. Alternatively the soft X-ray emission is absorbed by [O III] gas in the LOS in these dense regions. Deeper X-ray observations would allow comparison of this ratio on smaller spatial scales with a useful signal-to-noise ratio.

5.7 STIS kinematic profiles

The G430L and G750M spectra display a wavelength offset of 2.5 Å (150 km s^{-1}) based on comparison of the redshift of Hα and Hβ lines, which is corrected for in our [O III] velocity profiles. The source of this shift is unclear and appears in both the archival and reprocessed spectra.

The velocities and line widths of the emission lines are consistent with either gravitational motion of gas around the galaxy, given the velocity FWHM of up to ≈300 km s^{-1} observed in the Hα emission. Given that NGC 5972 is likely a post-merger system, the observed complex velocity profiles may be the result of perturbed kinematics induced by galaxy interaction rather than evidence of any larger scale outflow. Given the evidence for shocked gas from the soft X-ray emission, the dynamics inferred from the [O III] emission are surprisingly quiescent. The resolved structure of the bubble limits the velocity resolution we can achieve to ≈ 640 km s^{-1}, which while considerably worse than the Hα resolution is still below the measured [O III] FWHMs of Type II AGN hosting AGN-driven outflows. For example, Fischer et al. (2018) observed [O III] kinematics of 12 Type II QSO's, finding broader emission lines and larger velocity offsets, with FWHMs up to 1500 km s^{-1} (Fischer et al. 2018). Given their classification scheme (Section 3.2), our upper limit on the observed [O III] emission is fully consistent with 'disturbed rotation', which could purely be driven by post-merger gravitational interactions. Some comparison can be of the kinematics within the bubble are comparable to the bubbles seen within the Teacup (Harrison et al. 2015), with similarly low velocity offsets but resolved [O III] FWHMs $>$ 700 km s^{-1}, which is larger than we measure within the [O III] bubble but perhaps more comparable that the Type II QSO's studied in Fischer et al. (2018). We also note that the implied crossing time of the eastern bubble in the Teacup is comparable to our estimate for the bubble in NGC 5972, perhaps suggesting a characteristic lifetime for these structures.

The radial velocity of the [O III] gas peaks at ∼300 km s^{-1}, which is not strong enough to drive shocks in the main thermal component (APEC$_1$) unless it is a component of the true velocity of the outflow due to LOS projection effects. The 780 km s^{-1} outflow suggested by the double APEC model may be strong enough to drive fast shocks capable of photoionizing the precursor material. Our spectra may not be deep enough to measure the redshifted [O III], which could be heavily obscured, or the bubble may contain a multiphase medium with distinct populations that weakly collimate each other. Based on the addition of a second Gaussian component the best fit of Hα emission integrated over the central 0.2 arcsec shows evidence for a secondary population of gas with a 200 km s^{-1} blueshift, which may indicate dynamically perturbed gas or a weak outflow. In the *HST* images of the [O III] bubble, particularly Fig. 1, we observe a number of small scale structures within the bubble itself, indicated by regions of varying surface brightness. These may be indicative of smaller bubble or loop-like filaments embedded within the main structure. The STIS slit location passes through several of these features, which may be complicating our observed velocity profile across the bubble. These bubble-like structures may be indicative of outflow variations or due to variable extinction across the bubble, causing small-scale [O III] reddening. Fischer et al. (2013) discuss models to constrain opening angle and orientation based on observed velocity profiles of NLR gas. Our velocity profile is more complex than predicted by their models, but they do suggest asymmetries in the velocity profile can sometimes be explained by LOS sampling effects.

5.8 Kinematic comparisons

Keel et al. (2015, 2017) and Finlez et al. (2022) have both analysed the kinematics of the central region of NGC 5972 using 2D and 3D velocity maps derived from IFU spectroscopy and Fabry–Perot interferometric (FPI) data. We can make comparisons between their work and the velocity profiles we derive from the STIS slit spectroscopy. Overall we find good agreement with the kinematics, Keel et al. (2017) observe, given the differences in resolution between the ground-based IFU data and the *Hubble* STIS observations. The Gemini Multiple-Object Spectrometer (GMOS) data presented by Keel et al. (2017; fig. 12), shows the ≈100 km s^{-1} blueshift of the Hα line emission in the nucleus. Given the limits on the velocity resolution due to the extended structure of the bubble, we cannot resolve the velocity dispersion measurements seen in the GMOS map (≈ 100 km s^{-1}) or in the FPI data (130 km s^{-1} in [O III]5008 Å).

Finlez et al. (2022) have used the MUSE instrument on the Very Large Telescope to do wide-field integral field spectroscopy of NGC 5972. Our results are broadly consistent with the velocity maps they observe. Within the central region they see evidence of outflows up to 300 km s^{-1}, but are limited by the instrumental spectral resolution of MUSE. We see similar velocities within the Hα emission, but cannot make a comparison to the [O III]5008 Å emission due to the velocity resolution of the grating. Finlez et al. (2022) also suggest that the observed velocity profiles from MUSE are consistent with perturbed kinematics induced by galaxy interactions.

6 CONCLUSIONS

In this paper we present new *Chandra* ACIS X-ray observations of NGC 5972 alongside new *HST* STIS spectroscopy. NGC 5972 is one of the 19 'Voorwerpjes' galaxies, with an EELR that has been used as a quasar light echo to infer a 2.1 dex decrease in bolometric luminosity over the last 50 kyr. We detect broad-band X-ray emission from NGC 5972 coincident with an arcsecond scale bubble-like structure seen in *HST* [O III] imaging which contains the central engine. Simulations of the *Chandra* PSF show that the soft emission (0.5–1.5 keV) is spatially extended out to 2.5 arcsec in the same direction as the bubble. Spectral modelling shows that the soft emission is compatible with a combination of photoionized and collisionally ionized gas. One model suggests two populations of collisionally ionized gas with temperatures of ∼0.80 and ∼0.1 keV. From this model we have been able to estimate other physical parameters, including the effects of feedback on the ISM. We

Downloaded from https://academic.oup.com/mnras/article/526/3/4174/7288715 by Cal Polytechnic State Univ San Luis Obispo user on 29 November 2023

calculate an age of the bubble of at least ∼2 Myr, much longer than the current variability time-scale (∼ 50 kyr). We find evidence of efficient feedback, with ratios of kinetic power to bolometric luminosity of ∼1 per cent, indicative of feedback strong enough to drive out the gas on long time-scales under a two-stage feedback model. We discuss the possibility that this ratio is overestimated given the known decrease in the bolometric luminosity on time-scales much shorter than the crossing time of the bubble.

The STIS spectroscopy has allowed us to probe the kinematics of the gas across the bubble. Given the extended structure of the [O III] region we are limited by the velocity resolution of a filled slit in the G430L and G750M filters, but we find relatively quiescent kinematics from the fitted emission-line FWHMs which are consistent with perturbed kinematics induced by galaxy interactions. The velocity broadening of the [O III] emission is not resolved, giving an upper limit of ≈640 km s^{-1}, which is lower than observed in many Type II QSO's which host outflows (Fischer et al. 2018). As we do not observe the large linewidths associated with outflows in many AGN (e.g. NGC 1068, Das et al. 2006), we do not find evidence for comparable outflows in NGC 5972. We see velocity offsets of up to 300 km s^{-1} in the [O III] emission, which is unlikely to be strong enough to drive an outflow that can shock the X-ray emitting gas unless the measured radial velocity is only be a component of the 780 km s^{-1} outflow implied by the higher temperature gas, given an LOS projection effect. The overall unsymmetrical velocity profile is complex and not well explained by a simple outflow model, which may partly be explained by an LOS projection effect.

NGC 5972 shows misalignment on multiple spatial scales, including the jets, lobes and EELRs, which is not well explained by the traditional simplistic AGN model. The current radio jets, seen in VLASS data, are not aligned with the radio lobes, which is similar to the misalignment seen in 'restarted' radio AGN. Like a majority of the 'Voorwerpjes' galaxies, NGC 5972 shows evidence, such as tidal tails, of a recent merger or significant interaction. On a smaller scale, the long axis of the [O III] and X-ray structure is perpendicular to the bi-cone, which is aligned with the EELRs. These results might imply the presence of a double SMBH, which could support a more complex system of outflows, jets, and lobes.

We detect soft X-ray emission from diffuse warm gas coincident with the [O III] EELRs. Ratios of [O III] to soft X-ray flux are comparable to those seen in other EELRs. Spectral analysis of these EELRs is consistent with a photoionizing source, but deeper X-ray observations are required to constrain the model parameters and make better morphological comparison to the [O III] emission.

Much of our analysis is limited by the depth of the X-ray observations. With a longer *Chandra* observation of a few hundred ks, we would be able to simultaneously probe the extended soft emission from the EELR as well as de-convolve the hard X-ray emission from the nucleus in order to confirm the nuclear source centroid and extent with better accuracy. It may be possible to estimate the historic variability on Myr time-scales using the soft X-ray emission from the EELRs as a light echo, as has been done for HV. Probing longer time-scales than is possible using optical EELR lets us average over multiple duty cycles, to probe the time-scales of extended jets and radio lobe formation.

ACKNOWLEDGEMENTS

TH would like to thank the University of Southampton and the Center for Astrophysics| Harvard & Smithsonian, where this research was carried out. WPM acknowledges support by *Chandra* grants GO8-19096X, GO5-16101X, GO7-18112X, and GO8-19099X, and *Hubble* grant HST-GO-15350.001-A. VNB gratefully acknowledges assistance from National Science Foundation (NSF) Research at Undergraduate Institutions (RUI) grants AST-1909297. Note that findings and conclusions do not necessarily represent views of the NSF. AM was supported by the SAO RAS government contract approved by the Ministry of Science and Higher Education of the Russian Federation. LFS acknowledges the financial support of the Swiss National Science Foundation. This research is based on observations made with the NASA/ESA *Hubble Space Telescope* obtained from the Space Telescope Science Institute, which is operated by the Association of Universities for Research in Astronomy, Inc., under NASA contract NAS 5–26555. CF acknowledges support from FONDECYT through Postdoctoral grants 3220751. This research has made use of data obtained from the Chandra Data Archive and the Chandra Source Catalog, and software provided by the Chandra X-ray Center (CXC) in the application packages CIAO and Sherpa.

DATA AVAILABILITY

The raw data products used in this analysis are publicly available on the *Chandra* Data Archive (cxc.cfa.harvard.edu/cda) and the *Hubble* Legacy Archive (hla.stsci.edu). Data products produced for this paper will be provided on reasonable request to the authors.

REFERENCES

Ahumada R. et al., 2020, ApJS, 249, 3
Alexander D. M., Hickox R. C., 2012, New Astron. Rev., 56, 93
Allen C., Jerius D. H., Gaetz T. J., 2004, in Flanagan K. A., Siegmund O. H. W., eds, Proc. SPIE Conf. Ser. Vol. 5165, X-Ray and Gamma-Ray Instrumentation for Astronomy XIII. SPIE, Bellingham, p. 423
Andretta V., Busà I., Gomez M., Terranegra L., 2005, A&A, 430, 669
Baldwin J. A., Phillips M. M., Terlevich R., 1981, PASP, 93, 5
Baloković M., García J. A., Cabral S. E., 2019, Res. Notes Am. Astron. Soc., 3, 173
Belloni T. M., 2010, in Lecture Notes in Physics, Vol. 794, The Jet Paradigm: From Microquasars to Quasars. Springer-Verlag, Berlin Heidelberg, p. 53
Bennert N., Falcke H., Schulz H., Wilson A. S., Wills B. J., 2002, ApJ, 574, L105
Bianchi S., Guainazzi M., Chiaberge M., 2006, A&A, 448, 499
Bîrzan L., Rafferty D. A., McNamara B., Wise M., Nulsen P. E., 2004, ApJ, 607, 800
Bogdán Á., Kraft R. P., Evans D. A., Andrade-Santos F., Forman W. R., 2017, ApJ, 848, 61
Campanelli M., Lousto C., Zlochower Y., Merritt D., 2007, ApJ, 659, L5
Cappellari M., 2017, MNRAS, 466, 798
Carter C., Karovska M., Jerius D., Glotfelty K., Beikman S., 2003, in Payne H. E., Jedrzejewski R. I., Hook R. N., eds, ASP Conf. Ser. Vol. 295, Astronomical Data Analysis Software and Systems XII. Astron. Soc. Pac., San Francisco, p. 477
Chambers K. C. et al., 2016, preprint (arXiv:1612.05560)
Condon J. J., Cotton W., Greisen E., Yin Q., Perley R. A., Taylor G., Broderick J., 1998, ApJ, 115, 1693
Das V., Crenshaw D., Kraemer S., Deo R., 2006, AJ, 132, 620
Davis J. E. et al., 2012, in Takahashi T., Murray S. S., den Herder J.-W. A., eds, Proc. SPIE Conf. Ser. Vol. 8443, Space Telescopes and Instrumentation 2012: Ultraviolet to Gamma Ray. SPIE, Bellingham, p. 84431A
Di Matteo T., Springel V., Hernquist L., 2005, in Merloni A., Nayakshin S., Sunyaev R. A., eds, Growing Black Holes: Accretion in a Cosmological Context. Berlin, Springer, p. 340
Dickey J. M., Lockman F. J., 1990, ARA&A, 28, 215
Doe S. et al., 2007, in Shaw R. A., Hill F., Bell D. J., eds, ASP Conf. Ser. Vol. 376, Astronomical Data Analysis Software and Systems XVI. Astron. Soc. Pac., San Francisco, p. 543
Done C., Gierliński M., Kubota A., 2007, A&AR, 15, 1

Downloaded from https://academic.oup.com/mnras/article/526/3/4174/7288715 by Cal Polytechnic State Univ San Luis Obispo user on 29 November 2023

Eckersall A. J., Vaughan S., Wynn G. A., 2015, MNRAS, 450, 3410
Elvis M., 2000, ApJ, 545, 63
Eracleous M., Lewis K. T., Flohic H. M., 2009, New Astron. Rev., 53, 133
Fabbiano G., Paggi A., Karovska M., Elvis M., Maksym W., Risaliti G., Wang J., 2018, ApJ, 855, 131
Fabbiano G., Elvis M., Fabbiano G., Elvis M., 2019, ApJ, 884, 163
Fabian A. C., 1999, MNRAS, 308, L39
Fabian A., 2012, ARA&A, 50, 455
Falcón-Barroso J., Sánchez-Blázquez P., Vazdekis A., Ricciardelli E., Cardiel N., Cenarro A. J., Gorgas J., Peletier R. F., 2011, A&A, 532, A95
Ferland G., Korista K., Verner D., Ferguson J., Kingdon J., Verner E., 1998, PASP, 110, 761
Finlez C. et al., 2022, ApJ, 936, 88
Fischer T. C., Crenshaw D. M., Kraemer S. B., Schmitt H. R., 2013, ApJS, 209, 1
Fischer T. C. et al., 2018, ApJ, 856, 102
Fruscione A. et al., 2006, in Silva D. R., Doxsey R. E., eds, Proc. SPIE Conf. Ser. Vol. 6270, Observatory Operations: Strategies, Processes, and Systems. SPIE, Bellingham, p. 62701V
Gandhi P., Hönig S. F., Kishimoto M., 2015, ApJ, 812, 113
Gaskin J. A. et al., 2018, in Proc. SPIE Conf. Ser. Vol. 10699, Space Telescopes and Instrumentation 2018: Ultraviolet to Gamma Ray. SPIE, Bellingham, p. 106990N
Gebhardt K. et al., 2000, ApJ, 539, L13
Groves B. A., Allen M. G., 2010, New Astron., 15, 614
Groves B. A., Dopita M. A., Sutherland R. S., 2004, ApJS, 153, 75
Groves B., Brinchmann J., Walcher C. J., 2012, MNRAS, 419, 1402
Harrison C., Thomson A., Alexander D., Bauer F. E., Edge A., Hogan M., Mullaney J., Swinbank A., 2015, ApJ, 800, 45
Hodges-Kluck E. J., Reynolds C. S., Miller M. C., Cheung C. C., 2010, ApJ, 717, L37
Hopkins P. F., Elvis M., 2009, MNRAS, 401, 7
Hopkins P. F., Hernquist L., Cox T. J., Robertson B., Krause E., 2007, ApJ, 669, 67
Kashyap V., 2010, Analysis of Chandra PSF feature using ACIS data, available at: https://cxc.harvard.edu/cal/Hrc/PSF/acis_psf_2010oct.html (Accessed 2021 May)
Kauffmann G. et al., 2003, MNRAS, 346, 1055
Keel W. C. et al., 2012a, AJ, 144, 66
Keel W. C. et al., 2012b, MNRAS, 420, 878
Keel W. C. et al., 2015, AJ, 149, 155
Keel W. C. et al., 2017, ApJ, 835, 256
Komossa S., Burwitz V., Hasinger G., Predehl P., Kaastra J. S., Ikebe Y., 2003, ApJ, 582, L15
Körding E. G., Jester S., Fender R., 2006, MNRAS, 372, 1366
Koss M. J. et al., 2016, ApJ, 824, L4
Lacy M. et al., 2020, PASP, 132, 035001
Levesque E. M., Richardson M. L., 2013, ApJ, 780, 100
Li J., Kastner J. H., Prigozhin G. Y., Schulz N. S., Feigelson E. D., Getman K. V., 2004, ApJ, 610, 1204
Liang Y.-C., Hammer F., Flores H., Gruel N., Assémat F., 2004, A&A, 417, 905
Lintott C. J. et al., 2009, MNRAS, 399, 129
Livio M., 1999, Phys. Rep., 311, 225
Maccarone T. J., Gallo E., Fender R., 2003, MNRAS, 345, L19
Magorrian J. et al., 1998, AJ, 115, 2285
Maksym W. P., Fabbiano G., Elvis M., Karovska M., Paggi A., Raymond J., Wang J., Storchi-Bergmann T., 2017, ApJ, 844, 69
Maksym W. P. et al., 2019, ApJ, 872, 94
Maksym W. P. et al., 2021, ApJ, 917, 85
Mathur S., Stoll R., Krongold Y., Nicastro F., Brickhouse N., Elvis M., 2009, in Heinz S., Wilcots E., eds, AIP Conf. Proc. Vol. 1201, The Monster's Fiery Breath: Feedback in Galaxies, Groups, and Clusters. AIP Publishing, New York, p. 33
McCully C et al., 2018, astropy/astroscrappy: v1.0.5. Zenodo, available at: https://zenodo.org/record/1482019
McHardy I., Koerding E., Knigge C., Uttley P., Fender R., 2006, Nature, 444, 730
McKee C. F., Ostriker J. P., 1977, ApJ, 218, 148
McNamara B. R., Nulsen P. E. J., 2012, New J. Phys., 14, 055023
Merritt D., Ekers R. D., 2002, Science, 297, 1310
Mingozzi M. et al., 2019, A&A, 622, A146
Mukherjee D., Wagner A. Y., Bicknell G. V., Morganti R., Oosterloo T., Nesvadba N., Sutherland R. S., 2018, MNRAS, 476, 80
Netzer H., 2019, MNRAS, 488, 5185
Paggi A., Wang J., Fabbiano G., Elvis M., Karovska M., 2012, ApJ, 756, 39
Prichard L., Welty D., Jones A., 2022, STIS Instrument Handbook for Cycle 30, Vol. 21. STScI, Baltimore, p. 21
Raga A. C., Noriega-Crespo A., Velázquez P. F., 2002, ApJ, 576, L149
Remillard R. A., McClintock J. E., 2006, ARA&A, 44, 49
Reynolds C. S., 2012, ApJ, 759, L15
Richardson C. T., Allen J. T., Baldwin J. A., Hewett P. C., Ferland G. J., 2014, MNRAS, 437, 2376
Rubinur K., Das M., Kharb P., Honey M., 2017, MNRAS, 465, 4772
Saripalli L., Malarecki J. M., Subrahmanyan R., Jones D. H., Staveley-Smith L., 2013, MNRAS, 436, 690
Sartori L. F. et al., 2016, MNRAS, 457, 3629
Sartori L. F., Schawinski K., Trakhtenbrot B., Caplar N., Treister E., Koss M. J., Megan Urry C., Zhang C., 2018, MNRAS, 476, L34
Schawinski K. et al., 2010, ApJ, 724, L30
Schawinski K., Koss M., Berney S., Sartori L. F., 2015, MNRAS, 451, 2517
Shankar F., Weinberg D. H., Miralda-Escudé J., 2009, ApJ, 690, 20
Shen Y., Loeb A., 2010, ApJ, 725, 249
Silk J., Rees M. J., 1998, A&A, 331, L1
Skipper C. J., McHardy I. M., 2016, MNRAS, 458, 1696
Smith R. K., Brickhouse N. S., Liedahl D. A., Raymond J. C., 2001, ApJ, 556, L91
Soltan A., 1982, MNRAS, 200, 115
Stockton A., Fu H., Canalizo G., 2006, New Astron. Rev., 50, 694
Storchi-Bergmann T., Schmitt H. R., Calzetti D., Kinney A. L., 1998, AJ, 115, 909
van Dokkum P. G., 2001, PASP, 113, 1420
Vantyghem A. N., McNamara B. R., Russell H. R., Main R. A., Nulsen P. E. J., Wise M. W., Hoekstra H., Gitti M., 2014, MNRAS, 442, 3192
Vazdekis A., Sánchez-Blázquez P., Falcón-Barroso J., Cenarro A. J., Beasley M. A., Cardiel N., Gorgas J., Peletier R. F., 2010, MNRAS, 404, 1639
Veron P., Veron-Cetty M. P., 1995, A&A, 296, 315
Voggel K. T. et al., 2022, A&A, 658, A152
Wang J., Fabbiano G., Karovska M., Elvis M., Risaliti G., Zezas A., Mundell C., 2009, ApJ, 704, 1195
Wang J. et al., 2011, ApJ, 742, 23
Yu Q., Tremaine S., 2002, MNRAS, 335, 965
Zhao X., Marchesi S., Ajello M., Cole D., Hu Z., Silver R., Torres-Albà N., 2021, A&A, 650, A57
Zhou H., Wang T., Zhang X., Dong X., Li C., 2004, ApJ, 604, L33

APPENDIX A: 2D SPECTRA

Figs A1 and A2 show the 2D spatially resolved spectra for both gratings, where the horizontal axis corresponds to wavelength and the vertical axis is spatial offset. The spectral regions corresponding to bright emission lines are labelled, and a scale for both axes is shown.

Downloaded from https://academic.oup.com/mnras/article/526/3/4174/7288715 by Cal Polytechnic State Univ San Luis Obispo user on 29 November 2023

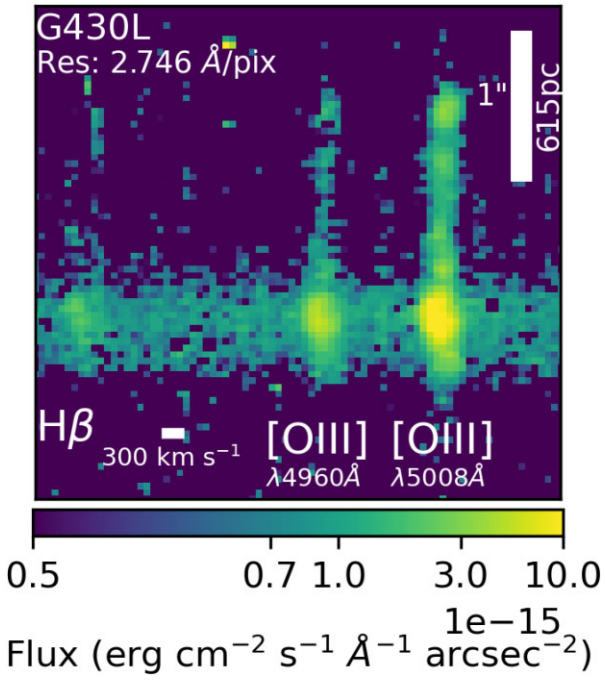

Figure A1. 2D spatially resolved spectra of the nuclear bubble showing the [O III]5008 and 4960 Å emission-line profiles from the *HST* G430L observation. The horizontal (wavelength) scale is shown in velocity units, and the vertical (spatial) scale is indicated in arcseconds and parsec. A logarithmically scaled colour bar indicates the flux of each pixel.

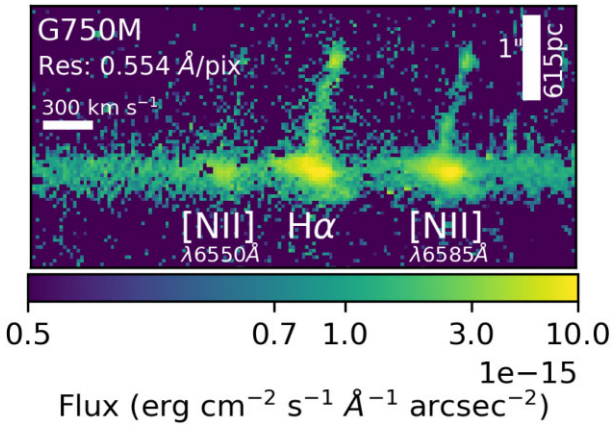

Figure A2. 2D spatially resolved spectra of the nuclear bubble showing the Hα, [N II]6550 and 6585 Å emission-line profiles from the *HST* G750M observation. The horizontal (wavelength) scale is shown in velocity units, and the vertical (spatial) scale is indicated in arcseconds and parsec. A logarithmically scaled colour bar indicates the flux of each pixel.

This paper has been typeset from a TEX/LATEX file prepared by the author.

Downloaded from https://academic.oup.com/mnras/article/526/3/4174/7288715 by Cal Polytechnic State Univ San Luis Obispo user on 29 November 2023

© 2023 The Author(s)
Published by Oxford University Press on behalf of Royal Astronomical Society. This is an Open Access article distributed under the terms of the Creative Commons Attribution License (http://creativecommons.org/licenses/by/4.0/), which permits unrestricted reuse, distribution, and reproduction in any medium, provided the original work is properly cited.